Numerical modelling of wrinkled hyperelastic membranes with topologically complex internal boundary conditions

Numerical modeling of wrinkled hyperelastic membranes with topologically complex internal boundary conditions

R. Alberini[a], A. Spagnoli[a,*], M. Terzano[b]

[a] *Department of Engineering and Architecture, University of Parma, Parco Area delle Scienze 181/A, 43124 Parma, Italy*
[b] *Institute of Biomechanics, Graz University of Technology, Stremayrgasse 16/II, 8010 Graz, Austria*

Abstract

Several soft biological tissues and artificial materials are characterised by a mechanical behaviour described by two-dimensional structural systems sustaining in-plane forces. Within the framework of finite strain elasticity, in this paper the formulation and finite element implementation of a hyperelastic incompressible membrane is presented. Focus is placed on the behaviour of membranes presenting holes and internal cuts. A new efficient algorithm is presented to describe topologically complex internal boundaries along which dislocation-like distributions are prescribed, so as to allow a one-to-one progressive joining of boundary material points. The classical Ogden's model is modified into a relaxed version in order to accommodate the no-compression response of thin membranes due to wrinkling. Three applicative examples are presented to illustrate the potential of the method proposed.

Keywords: membrane; wrinkling; dislocation; internal boundary condition;

*Corresponding author
Tel.: +39 0521 905927
e-mail: spagnoli@unipr.it

hyperelasticity; Z-plasty

1. Introduction

Soft membranes can be encountered at different scales, both in natural systems and in several engineering applications. In biology, membranes fulfil crucial physiological needs. From cellular walls at the micro scale, to skin in living beings at the macro scale, biological membranes act as protection against external hazards [1]. Thanks to osmosis, membranes also regulate chemical exchanges between external and internal environment, maintaining optimal conditions, e.g. ph, moisture and temperature, within the enclosed domain [2]. Synthetic membranes are largely employed in medicine, for hygiene devices, bio-mimicking tissues [3], tapes and tubes [4]. In recent years, various kinds of membrane structures have been developed for applications in new technologies to meet specific requirements, including, for instance, batteries [5] and supercapacitors [6] for stretchable electronics.

By a mechanical point of view, soft membranes are lightweight structures exposed to large deformations and relevant in-plane strains [7]. An area of great interest concerns the behaviour of membranes presenting holes or cuts. As these are usually the result of damage, they should be healed in order to restore the continuity of the surface and the functionalities of the membrane [8]. This can be done by applying patches of the same size of the loss using external material, or by joining the boundaries of the discontinuity through proper displacements in order to make them coincident in the final configuration. With the latter method, since no new material is supplied, the way chosen for the closure procedure influences the rearrangement of the stress and strain fields in the neighbourhood of the hole. Traditionally, in plastic surgery the suturing of scars has explored the different ways in which the joining process can be performed, in order to achieve the best aesthetic result [9]. However, this concept can also be exploited in a reversed way, such that desired distortions can be induced within the membrane by appropriately creating holes and related closures. In the field of metamaterials, for instance, holes closure is used in kirigami tessellation. By creating a suitable pattern of incisions on a flat sheet, the closure of holes produces a coordinated movement of interconnected tiles, which deploys the sheet in a different and reversible shape [10–12].

In mechanical terms, the process of inducing distortions through the application of internal boundary conditions in a soft membrane generates a state of self-balanced stress within the domain, with higher stresses concentrated in the neighborhood of the inner boundaries. The problem involves both large strains and displacements, making numerical methods the most appealing tool of analysis. A first attempt to study the mechanical behaviour of biological membranes embedding closing holes was carried out by Larrabee and Galt [13], who used the Finite Element (FE) method to simulate the suturing of skin flaps. More recently, other authors have improved the analysis by employing non-linear material models and adopting different approaches to achieve closure. Lott-Crumpler and Chaudhry [14] and Flynn [15] achieved closure of symmetric holes by approaching nodes lying on two separate edges and making them coincide in the midway position. An alternative solution was proposed by Rajabi et al. [16], who simulated the closure of unsymmetric holes by coupling pairs of nodes on opposite edges with trusses, which were then shrunk through fictitious variations of temperature.

The main shortcoming of the available methods is the limited applicability to complex shapes of the internal boundary, in which the final configuration of the edges is a problem unknown, and no prescribed displacements can be applied on them. In order to achieve a perfect coincidence between two joining nodes, a suitable approach is to add kinematic equations in order to constrain nodes to move toward each other until the gap is null, e.g. via so-called multi-point constraints (MPCs) in FE models [17]. The approach is similar to that of Rajabi et al. [16], but without the drawbacks of trusses, which cannot reach vanishing lengths. Arbitrarily shaped cavities may include several critical points, making meshing and definition of the constraints difficult to be performed manually. Moreover, this task is further complicated by the fact that discretisation along the hole boundaries must be consistent, that is, nodes must be in equal number and uniformly distributed between two pairing edges. In order to conciliate the requirements for a consistent discretisation of domain boundaries with automatic meshing, the generation of FE models using a custom pre-processing code is deemed to be convenient.

As membranes are thin solids, compressive internal forces may lead to instabilities, resulting in out-of-plane displacements [18]. This phenomenon, known as *wrinkling*, is well known in biological tissues [19, 20] as well as in engineered materials [21–24]. In general, the study of wrinkling requires geometrically non-linear analyses: in order to determine the exact out-of-plane deflection of compressed membranes, the flexural buckling and post-buckling behaviour should be analysed [25–28]. However, if no specific information about wrinkle wavelength and amplitude is needed, a properly modified plane stress constitutive model can be adopted, in which the non-linearity induced by finite out-of-plane displacements is treated as a material non-linearity [29–33]. This represents a computationally efficient approach suitable to determine the in-plane tension field of the membrane, and precisely identify the distribution of wrinkled regions.

In this paper, a numerical model of soft membranes with topologically complex internal boundaries is presented. The algorithm is developed within the Matlab® environment and it is linked with the open source code DistMesh developed by Persson and Strang [34], which is capable of efficiently meshing any two-dimensional domain. The proposed algorithm allows general shapes of boundaries to be generated and complex dislocations distributions to be applied along them. Furthermore, a wrinkling constitutive model is proposed and implemented in a FE formulation in order to take into account the no-compression behaviour of the soft membrane. In particular, the formation of wrinkles is included through a relaxed strain-energy density, based on the hyperelastic Ogden's function. Although the constitutive law is isotropic, more general anisotropic formulations, which have been proposed for soft biological membranes [35, 36], can also be included.

The outline of the paper is as follows. Sect. 2 presents the fundamentals of the finite strain theory of soft membranes in which the hyperelastic constitutive model is developed. Wrinkling is accounted for by a proper modification of the hyperelastic potential. The linearised form of the constitutive equations is also presented for the FE implementation. Sect. 3 describes the definition of general boundary conditions along topologically complex internal boundaries of the membrane, where general dislocation distributions can be applied. Sect. 4 is devoted to the numerical implementation of the model. In particular, algorithms for automatic generation of FE models are presented, allowing the description of the topology of internal boundaries, accurate refined meshing and the application of general dislocation distributions along the boundaries. Sect. 5 presents three applicative cases concerning different soft membranes geometries. Comparisons with existing numerical and experimental data is included. Finally, Sect. 6 summarises the potential and limits of the proposed approach and presents concluding remarks.

2. Wrinkling hyperelastic membranes

2.1. Kinematics

Given a material body $\mathcal{B}$ occupying the region Ω at time $t_0 = 0$, any material point $P \in \mathcal{B}$ can be mapped from the reference position $\mathbf{X}$ to the current $\mathbf{x}$ according to the unique biunivocal function $\mathbf{x} = \chi(\mathbf{X}, t)$. The resulting deformation is described by the second-order tensor $\mathbf{F} = \partial\chi(\mathbf{X}, t)/\partial\mathbf{X} = \partial\mathbf{X}/\partial\mathbf{x}$, known as the deformation gradient. Membranes can be considered two-dimensional structural elements enforcing a condition of plane stress. In a co-rotational orthonormal system, defined by the in-plane basis vectors $\mathbf{e}_1, \mathbf{e}_2$ and the normal vector $\mathbf{e}_3$, the deformation gradient is therefore written as

$$\mathbf{F} = \begin{bmatrix} F_{11} & F_{12} & 0 \\ F_{21} & F_{22} & 0 \\ 0 & 0 & (F_{11}F_{22} - F_{12}F_{21})^{-1} \end{bmatrix} \tag{1}$$

where the assumption of incompressibility $J = \det \mathbf{F} = 1$ was introduced.

For later use in the formulation of the constitutive model of the wrinkled membrane, the deformation gradient is decomposed according to $\mathbf{F} = \mathbf{R}\mathbf{U} = \mathbf{v}\mathbf{R}$, where $\mathbf{R}$ is an orthogonal rotation tensor, while $\mathbf{U}$ and $\mathbf{v}$ represent the symmetric stretch tensors, defined for the reference and the current configuration, respectively. Through spectral decomposition these tensors can be written as

$$\mathbf{U} = \sum_{a=1}^{3} \lambda_a \hat{\mathbf{N}}_a \otimes \hat{\mathbf{N}}_a, \quad \mathbf{v} = \sum_{a=1}^{3} \lambda_a \hat{\mathbf{n}}_a \otimes \hat{\mathbf{n}}_a \tag{2}$$

in which the eigenvalues λ_a, $a = 1, 3$ represent the principal stretches, while the eigenvectors $\hat{\mathbf{N}}_a$ and $\hat{\mathbf{n}}_a$ represent the principal referential and spatial directions, respectively, and are related by $\hat{\mathbf{n}}_a = \mathbf{R}\hat{\mathbf{N}}_a$. Finally, we define the spatial velocity gradient as $\mathbf{l} = \partial \mathbf{v}(\mathbf{x}, t)/\partial \mathbf{x} = \mathbf{d} + \mathbf{w}$, where $\mathbf{d}$ and $\mathbf{w}$ represent the symmetric rate of strain tensor and the antisymmetric spin tensor, respectively [37].

2.2. Constitutive model

In this work the membrane tissue is assumed to be homogeneous, hyperelastic and isotropic. A strain energy density function Ψ, provided by the well-known Ogden model [38], is introduced, which with the assumption of incompressibility ($J = \lambda_1 \lambda_2 \lambda_3 = 1$) is given by

$$\Psi = \sum_{i=1}^{N} \frac{\mu_i}{\alpha_i} \left(\lambda_1^{\alpha_i} + \lambda_2^{\alpha_i} + \lambda_3^{\alpha_i} - 3\right) - p\,(J-1) = \Psi_O(\lambda_1, \lambda_2, \lambda_3) - p\,(J-1) \tag{3}$$

where μ_i and α_i are material properties, whereas p is an unknown hydrostatic pressure introduced as a Lagrange multiplier to enforce the incompressibility constraint. Usually, a single set of parameters ($N = 1$) gives a good approximation to the J-shaped stress-strain curves commonly encountered in soft tissues [39].

The second Piola-Kirchhoff (PKII) stress tensor is written in terms of the principal stresses as

$$\mathbf{S} = \sum_{a=1}^{3} S_a \hat{\mathbf{N}}_a \otimes \hat{\mathbf{N}}_a \tag{4}$$

where the principal stress in the material configuration is $S_a = {\lambda_a}^{-1} \partial\Psi / \partial\lambda_a$. Through a standard push-forward operation to the current configuration, the Cauchy stress tensor reads

$$\boldsymbol{\sigma} = \sum_{a=1}^{3} \sigma_a \hat{\mathbf{n}}_a \otimes \hat{\mathbf{n}}_a, \quad \sigma_a = J^{-1} \lambda_a \frac{\partial\Psi}{\partial\lambda_a} \tag{5}$$

In order to compute the Lagrange multiplier p, the out-of-plane principal stress σ_3 must be set to zero in Eq. (5), that is,

$$\sigma_3 = \lambda_3 \frac{\partial\Psi_O}{\partial\lambda_3} - p = 0 \tag{6}$$

from which we find

$$p = \lambda_3 \frac{\partial\Psi_O}{\partial\lambda_3} = \sum_{i=1}^{N} \mu_i \left(\lambda_1 \lambda_2\right)^{-\alpha_i} \tag{7}$$

Combining Eqs. (5)-(7), the principal Cauchy stresses become

$$\sigma_a = \sum_i \mu_i \left(\lambda_a^{\alpha_i} - (\lambda_1 \lambda_2)^{-\alpha_i} \right), \quad a = 1, 2 \tag{8}$$

2.3. Wrinkling

The wrinkling behaviour when membranes are subjective to compressive states can be conveniently defined in terms of the principal stretches. Taking λ_1 as the reference stretch, there are three possible strain configurations for the membrane, depending on λ_2. A modified strain-energy function Ψ_W can be defined, depending on the configuration. This procedure, which somehow treats the out-of-plane deflection as a constitutive material non-linearity, is known as quasi-convexification of Ψ [40].

When $\lambda_1 \geq 1$ and $\lambda_2 \geq \lambda_1^{-1/2}$, the lateral deformation λ_2 is greater than that due to Poisson contraction, obtained imposing $\sigma_2 = 0$ in Eq. (8). In this case, no wrinkling occurs as lateral stretches greater than $\lambda_1^{-1/2}$ provide positive stresses. This is the so-called *taut* condition (Fig. 1a), and the relative strain-energy function $\Psi_W = \Psi$ is given by Eq. (3), with the incompressibility condition $J = 1$ (Fig. 1a).

If $\lambda_1 \geq 1$ and $\lambda_2 < \lambda_1^{-1/2}$, the membrane is actually compressed in the lateral direction, resulting in a *wrinkling* condition (Fig. 1b). Wrinkles parallel to λ_1 direction develop, carrying no loads along their orthogonal direction. Keeping fixed λ_1, further reductions of λ_2 do not increase the strain-energy, which remains equal to the minimum reached in the uniaxial stress state. Following the works of Evans [32] and Massabò and Gambarotta [41], Ψ_W depends only on λ_1, and can be obtained substituting $\lambda_2 = \lambda_1^{-1/2}$ into Eq. (3). Thus, we find

$$\Psi_W = \sum_{i=1}^{N} \frac{\mu_i}{\alpha_i} \left(\lambda_1^{\alpha_i} + 2\lambda_1^{-\frac{\alpha_i}{2}} - 3 \right) \tag{9}$$

Finally, if $\lambda_2 < \lambda_1 < 1$ the membrane is *slack* (Fig. 1c) and does not carry any load. No energy is stored within the material under loading, and hence the associated strain-energy function is set to zero.

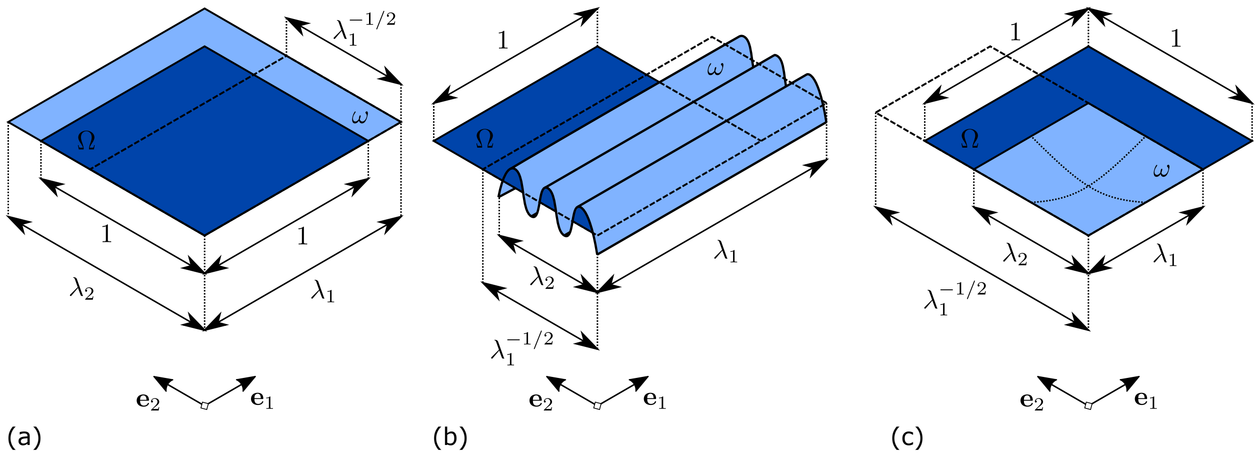

Figure 1. Reference Ω and deformed ω configuration of a unit membrane element. (a) Taut, (b) wrinkled and (c) slack configurations.

The function Ψ_W, summarised in Tab. 1 for both cases of $\lambda_1 > \lambda_2$ and $\lambda_2 > \lambda_1$, is called the relaxed strain-energy density function. Such a function is employed below to compute the stress and stiffness tensors in the linearised approximation of the governing equations.

2.4. Stress and elasticity tensors

Numerical solution methods for nonlinear problems are based on an incremental procedure, in which the principle of virtual work is consistently

Condition	Criteria	Relaxed strain-energy density
Taut (Fig. 1a)	$\lambda_1 \geq 1$ and $\lambda_2 \geq \lambda_1^{-1/2}$ or $\lambda_2 \geq 1$ and $\lambda_1 \geq \lambda_2^{-1/2}$	$\Psi_W = \sum_{i=1}^{N} \frac{\mu_i}{\alpha_i} \left(\lambda_1^{\alpha_i} + \lambda_2^{\alpha_i} + (\lambda_1 \lambda_2)^{-\alpha_i} - 3 \right)$
Wrinkled (Fig. 1b)	$\lambda_1 \geq 1$ and $\lambda_2 < \lambda_1^{-1/2}$	$\Psi_W = \sum_{i=1}^{N} \frac{\mu_i}{\alpha_i} \left(\lambda_1^{\alpha_i} + 2\lambda_1^{-\frac{\alpha_i}{2}} - 3 \right)$
	$\lambda_2 \geq 1$ and $\lambda_1 < \lambda_2^{-1/2}$	$\Psi_W = \sum_{i=1}^{N} \frac{\mu_i}{\alpha_i} \left(\lambda_2^{\alpha_i} + 2\lambda_2^{-\frac{\alpha_i}{2}} - 3 \right)$
Slack (Fig. 1c)	$\lambda_1 < 1$ and $\lambda_2 < 1$	$\Psi_W = 0$

Table 1. Relaxed strain-energy density function.

linearised with respect to displacements. This procedure also requires the linearisation of the constitutive relationship through the definition of a tangent stiffness matrix, in terms of the fourth-order elasticity tensor. In the spirit of an updated-Lagrangian method, where every increment is computed using the last equilibrium state as reference configuration, the elasticity tensor can be expressed in the spatial description through spectral decomposition as [37]

$$\begin{aligned} \mathbb{C}^{\boldsymbol{\tau}^\circ} = & \sum_{a,b=1}^{3} \lambda_a^2 \lambda_b \frac{\partial S_a}{\partial \lambda_b} \left(\hat{\mathbf{n}}_a \otimes \hat{\mathbf{n}}_a \otimes \hat{\mathbf{n}}_b \otimes \hat{\mathbf{n}}_b \right) + \\ & \sum_{a,b=1; a \neq b}^{3} \lambda_a^2 \lambda_b^2 \frac{S_b - S_a}{\lambda_b^2 - \lambda_a^2} \left(\hat{\mathbf{n}}_a \otimes \hat{\mathbf{n}}_b \otimes \hat{\mathbf{n}}_a \otimes \hat{\mathbf{n}}_b + \hat{\mathbf{n}}_a \otimes \hat{\mathbf{n}}_b \otimes \hat{\mathbf{n}}_b \otimes \hat{\mathbf{n}}_a \right) \end{aligned} \tag{10}$$

where $S_{a,b}$ are the principal PKII stresses of Eq. (4). The superscript $\boldsymbol{\tau}^{\circ}$ in the left term of Eq. (10) indicates that the elasticity tensor is in this way expressed in terms of the Oldroyd rate of the Kirchhoff stress tensor $\boldsymbol{\tau} = J\boldsymbol{\sigma}$.

Indeed, the linearised constitutive relationship must satisfy the principle of frame indifference. Different objective stress rates are available in the literature, most of them being based on the Lie time derivative and its linear combinations [42]. In particular, we here adopt the Jaumann rate of the Kirchhoff stress $\boldsymbol{\tau}^{\nabla} = \dot{\boldsymbol{\tau}} - \mathbf{w}\boldsymbol{\tau} + \boldsymbol{\tau}\mathbf{w} = \mathbb{C}^{\boldsymbol{\tau}^{\nabla}} : \mathbf{d}$, which is the co-rotational rate required by the commercial FE software ABAQUS employed in the analyses. Exploiting the relationship between Oldroyd and Jaumann rates, given by $\boldsymbol{\tau}^{\nabla} = \boldsymbol{\tau}^{\circ} + \mathbf{d}\boldsymbol{\tau} + \boldsymbol{\tau}\mathbf{d}$, the correct elasticity tensor $\mathbb{C}^{\boldsymbol{\tau}^{\nabla}}$ is computed as follows

$$\mathbb{C}^{\boldsymbol{\tau}^{\nabla}} = \mathbb{C}^{\boldsymbol{\tau}^{\circ}} + \boldsymbol{\tau} \odot \mathbf{I} + \mathbf{I} \odot \boldsymbol{\tau} \tag{11}$$

in which the operator $\odot$ denotes the symmetric dyadic product of second-order tensors, defined as $\{\bullet \odot \circ\}_{ijkl} = 1/2\left(\{\bullet\}_{ik}\{\circ\}_{jl} + \{\bullet\}_{il}\{\circ\}_{jk}\right)$ [43].

From Eq. (10), it can be noticed that using the relaxed Ogden function Ψ_W (Tab. 1), $\mathbb{C}^{\boldsymbol{\tau}^{\circ}}$ would result in zero stiffness in compression for wrinkled and slack regions, giving rise to ill-conditioning problems. This issue can numerically be circumvented by adding a small stiffness in compression by means of a fictitious tensor, computed from the standard strain-energy function of Eq. (3). Accordingly, the stiffness $\mathbb{C}^{\boldsymbol{\tau}^{\circ}}$ is additively decomposed as $\mathbb{C}^{\boldsymbol{\tau}^{\circ}} = \mathbb{C}_W^{\boldsymbol{\tau}^{\circ}} + \tilde{\mathbb{C}}^{\boldsymbol{\tau}^{\circ}}$, where $\mathbb{C}_W^{\boldsymbol{\tau}^{\circ}}$ and $\tilde{\mathbb{C}}^{\boldsymbol{\tau}^{\circ}}$ are the pure wrinkling and the fictitious stiffness tensors derived from Eq. (10). Specifically, the latter is obtained by considering the same constitutive Ogden model with a reduced stiffness, which ought to be small enough to have negligible influence on the tension field [32]. For the sake of simplicity, the stiffness of this sort of non-wrinkling fictitious layer is considered to depend on the first order coefficients of the original Ogden model, taking $\tilde{\mu}$ as a small fraction of μ_1, and $\tilde{\alpha}$ equal to α_1. This is equivalent to a uniform scaling of the original stress-stretch curve computed using the Ogden model. Test analyses are provided in Sect. 5 for a single plane stress element under uniaxial and biaxial strain conditions.

In the general case of an initial stress field $\boldsymbol{\sigma}_0$ acting across the domain Ω, stresses can no longer be computed using Eq. (5), but must be updated at each increment from the tensor $\mathbb{c}^{\boldsymbol{\tau}^\nabla}$ in the spatial description. Following Hughes and Winget [44], at each increment stresses $\boldsymbol{\sigma}_{n+1}$ are obtained by rotating $\boldsymbol{\sigma}_n$ from the reference configuration at increment n to the current, and then adding the co-rotational stress increment, which is obtained from the Jaumann rate of the Cauchy stress, namely

$$\boldsymbol{\sigma}_{n+1} = \boldsymbol{Q}_n \boldsymbol{\sigma}_n \boldsymbol{Q}_n^T + \mathbb{c}_n^{\boldsymbol{\sigma}^\nabla} : \delta \boldsymbol{\epsilon}_n \tag{12}$$

where $\boldsymbol{Q}_n$ is an incremental rotation tensor, $\mathbb{c}_n^{\boldsymbol{\sigma}^\nabla}$ is the elasticity tensor in terms of the Jaumann rate of the Cauchy stress, and $\delta \boldsymbol{\epsilon}_n$ is the incremental strain computed with the midpoint deformation rule from the rate of strain tensor $\mathbf{d}$ [45]. Knowing that $\boldsymbol{\sigma}^\nabla = J^{-1} \boldsymbol{\tau}^\nabla - (\mathbf{d} : \mathbf{I})\, \boldsymbol{\sigma}$ [45], the elasticity tensor appearing in Eq. (12) is obtained as

$$\mathbb{c}_n^{\boldsymbol{\sigma}^\nabla} = J^{-1} \mathbb{c}_n^{\boldsymbol{\tau}^\nabla} - \boldsymbol{\sigma}_n \otimes \mathbf{I} \tag{13}$$

where $\mathbb{c}_n^{\boldsymbol{\tau}^\nabla}$ is defined by Eq. (11) in combination with Eq. (10). Note that, in case of an initial pre-stress field $\boldsymbol{\sigma}_0$, at increment $n = 0$, $\boldsymbol{\sigma}_n$ is equal to $\boldsymbol{\sigma}_0$

and $\boldsymbol{Q}_n$ to the identity tensor in Eq. (12).

3. Internal boundaries with prescribed dislocations

In order to represent discontinuities in the elastic membranes, we introduce internal boundary conditions in addition to the usual ones in terms of prescribed tractions and displacements on the external boundaries. The type of internal boundary conditions here considered can be accommodated within the theory of *dislocations* (interested readers might refer to some fundamental papers on this theory, as for instance [46, 47] and the memorial paper on Eshelby's work [48]), which have to be intended as imposed relative displacements between points located on two different boundaries of a discontinuity. In other words, we consider cuts and holes — the latter implying a subtraction of material — embedded in the membrane, having general topologies, and prescribe relative displacements such that the boundaries formed by the cuts and holes are brought together and joined. The membrane will be in a state of self-balanced stress as a result of these internal boundary conditions.

Let suppose we place a distribution of dislocations along a number of internal boundaries $\partial\Omega^{I,n}$ in the membrane, each partitioned in pairs of subsets $\partial\Omega_i^{I,n+}$ and $\partial\Omega_i^{I,n-}$ which are joined together in the final configuration. Since, in general, the final topology of the subsets $\partial\omega_i^{I,n+}$ and $\partial\omega_i^{I,n-}$ is unknown, the prescribed displacements have to be expressed by introducing a constraint function Φ_i. Notice that subscripts and superscripts denote the n-th internal boundary and the i-th couple of paired subsets. Given the mapping function $\Gamma : \partial\Omega_i^{I,n+} \to \partial\Omega_i^{I,n-}$, which biunivocally relates every point $\mathbf{X}_i^+(\xi) \in \partial\Omega_i^{I,n+}$ with its counterpart $\mathbf{X}_i^-(\xi) \in \partial\Omega_i^{I,n-}$, the constraint consists in imposing the coincidence between the mapped points $\mathbf{x}_i^+(\xi) \in \partial\omega_i^{I,n+}$ and $\mathbf{x}_i^-(\xi) \in \partial\omega_i^{I,n-}$ after the motion χ (Fig. 2), where $\xi \in [0,1]$ biunivocally identifies the points $\mathbf{X}_i^+$, $\mathbf{X}_i^-$ (and $\mathbf{x}_i^+$,$\mathbf{x}_i^-$) in the subsets $\partial\Omega_i^{I,n+}, \partial\Omega_i^{I,n-}$ (and $\partial\omega_i^{I,n+}, \partial\omega_i^{I,n-}$). Knowing that $\mathbf{x} = \chi(\mathbf{X},t) = \mathbf{X} + \mathbf{u}(\mathbf{X},t)$, the constraint function is defined by

$$\Phi_i(\xi) = \mathbf{x}_i^+ - \mathbf{x}_i^- = \mathbf{X}_i^+ + \mathbf{u}(\mathbf{X}_i^+) - \Gamma(\mathbf{X}_i^+) - \mathbf{u}(\Gamma(\mathbf{X}_i^+)) = 0 \tag{14}$$

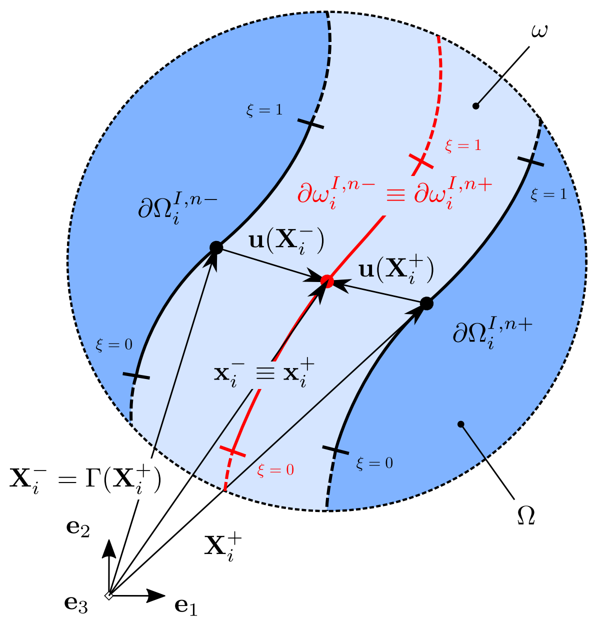

Figure 2. Schematics of joining dislocations applied to an internal boundary.

In order to achieve a full closure of a hole or cut, an even number $2N$ subsets must be considered, on which N functions $\Phi_i(\xi)$ are defined. Note that each i-th couple of subsets and the function Γ must be topologically consistent, i.e. they must not lead to knotted or intertwined surfaces. Then the discontinuity is closed by joining together the subsets encountered moving along the boundary from point $A \in \partial\Omega^{I,n}$ to point $B \in \partial\Omega^{I,n}$, so that a continuous line AB results. Note that subsets are ordered counter-clockwise starting from A, so that $\partial\Omega_i^{I,n+} = \partial\Omega_j^{I,n}$ and $\partial\Omega_i^{I,n-} = \partial\Omega_{2N-j+1}^{I,n}$, with $j = 1, ..., N$ (Fig. 3).

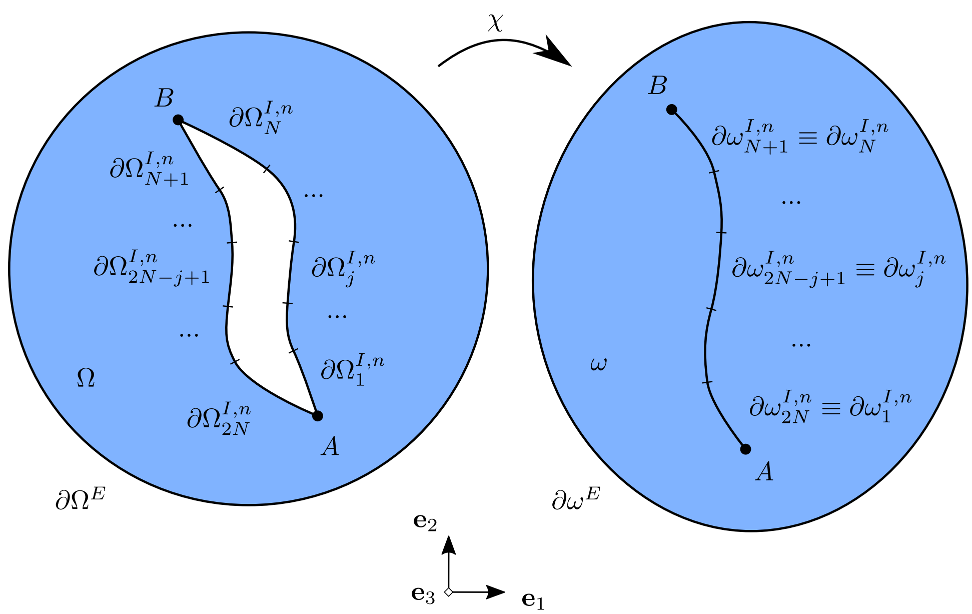

Figure 3. Complete closure of a single hole following a unique line from A to B. The internal boundary in the reference configuration has been divided into $2N$ subsets, numbered with counterclockwise order from the point A. The closure is achieved matching together the subsets at the right and left of the point A, such that each couple can be defined by the pairing rule $(\partial\Omega_{2N-j+1}^{I,n}, \partial\Omega_j^{I,n})$.

The mapping bijective function Γ has to be defined in order to apply a joining dislocation distribution along the internal boundary which precisely describe the physical problem under consideration. Generally speaking, the function Γ can conveniently be choseen to be linear so that $\|\mathrm{d}\mathbf{X}_i^{I,n-}\| =$

$c\,\|\mathrm{d}\mathbf{X}_i^{I,n+}\|$ for every ξ, where c is the ratio between the total lengths of $\partial\Omega_i^{I,n-}$ and $\partial\Omega_i^{I,n+}$. Except for trivial cases, such as the stitching of two overlapping edges, this kind of function Γ always generates a self-balanced stress state along the joining boundaries, which depends on their shape in the reference configuration.

4. Numerical implementation

The implementation of the model in a FE formulation, suitable to deal with the highly non-linear nature of the problem, is here described in detail. The membrane can be exposed to general displacements and tractions along the external boundary, to an initial pre-stress field $\boldsymbol{\sigma}_0$, and to complex dislocation distributions along the internal boundaries, as described in Sect. 3. Specifically, closed internal boundaries describing both cuts and holes in the membrane can be implemented. For the sake of simplicity, a single internal boundary $\partial\Omega^I$ will be considered, e.g. see Fig. 3.

In order to prescribe dislocation distributions along the internal boundary, the constraint represented by the function $\Phi_i(\xi)$ of Eq. (14) can be addressed in the finite element framework by imposing kinematic Multi-Point Constraints (MPCs) between pairs of nodes in an incremental form. Accordingly, the function $\Phi_i(\xi)$ is applied to each couple of nodes, belonging to $\partial\Omega_i^{I-}$ and $\partial\Omega_i^{I+}$, respectively.

The FE geometry can be obtained by an automatic meshing of the plane domain of the membrane, by means of dedicated algorithms that specify the element density near the regions of interest. However, although it is possible to obtain well meshed domains, the internal boundary $\partial\Omega^I$ may result in an uncontrolled distribution of nodes, raising issues in the MPC application when different number of nodes in the coupled boundaries $\partial\Omega_i^{I-}$ and $\partial\Omega_i^{I+}$ are encountered. Thus, the node spacing along the internal boundary becomes crucial when dislocation distributions are to be applied in a discretised manner. Therefore, a fully automatic procedure, which at the same time can generate the required dislocation distributions and ensure optimal meshing, is needed.

4.1. Topology of internal boundaries

We here describe the algorithm developed to automatically compute generic dislocation distributions along the internal boundaries. Let us assume that a certain domain can be represented by a signed distance function $d(\mathbf{X})$, which is the combination of closed geometrical entities obtained by multiple parametric curves. The external boundary $\partial\Omega^E$ usually consists of an elementary shape, like a circle or a rectangle. The internal boundary $\partial\Omega^I$ should be able to describe any complex closed topology. We define a set $\mathcal{V}_B^I$ of counter-clockwise vertices $\mathbf{X}_{B,j} \in \partial\Omega^I$ and approximate the curve through a linear piecewise function. Accordingly, the segment $\mathbf{X}_j^I(\xi) \in \partial\Omega_j^I$ is expressed by the linear Bézier curve

$$\mathbf{X}_j^I(\xi) = (1-\xi)\mathbf{X}_{B,j} + \xi\mathbf{X}_{B,j+1} \tag{15}$$

with $\xi \in [0,1]$. Note that the dislocation constraint Φ_i in Eq. (14) is defined between two sets $\partial\Omega_i^{I-}$ and $\partial\Omega_i^{I+}$, therefore $\mathcal{V}_B^I$ must contain $2N+1$ vertices, representing $2N$ subsets $\partial\Omega_j^I$.

In the case that $\partial\Omega^I$ represents a cut in the membrane, the different subsets are coincident and lie on the cut interface. This does not represent an issue from a geometrical point of view, but it can create difficulties in the auto-meshing, as elements might be generated across the cut. To circumvent this problem, the original boundary $\partial\Omega^I$ is offset externally by a quantity $s/2$, such that two facing subsets of a cut become spaced by s. We call the new boundary $\partial\overline{\Omega}^I$. The value of the spacing depends on the average element size. So, the vertices $\mathbf{X}_{S,j} \in \mathcal{V}_S^I$, representing the new offset boundary (Fig. 4a), are given by

$$\mathbf{X}_{S,j} = \mathbf{X}_{B,j} + \mathbf{s}_j^- + \mathbf{s}_j^+ \tag{16}$$

with

$$\mathbf{s}_j^- = \bar{s}\frac{\mathbf{X}_{B,j} - \mathbf{X}_{B,j-1}}{\|\mathbf{X}_{B,j} - \mathbf{X}_{B,j-1}\|} \times \mathbf{e}_3 \quad , \quad \mathbf{s}_j^+ = \bar{s}\frac{\mathbf{X}_{B,j+1} - \mathbf{X}_{B,j}}{\|\mathbf{X}_{B,j+1} - \mathbf{X}_{B,j}\|} \times \mathbf{e}_3 \tag{17}$$

where $\bar{s} = s/(2(1 + \cos\Delta\theta))$. Segments between two offset vertices are still defined by the linear curve in Eq.(15), using the new vertices $\mathbf{X}_S$ in place of $\mathbf{X}_B$.

When $\mathbf{X}_{B,j}$ represents a cut tip the preceding and following segments are parallel, characterized by $\Delta\theta = \pi$. This would make $\mathbf{X}_{S,j}$ to be placed at an infinite distance, as $\bar{s}$ degenerates to infinity for $\Delta\theta \to \pi$. In order to preserve the tip position, allowing us at the same time to create the offset of the internal boundary, the preceding and following segments can no longer be straight, and must be transformed into two curves which are parallel far from the tip, and converging in $\mathbf{X}_{S,j} = \mathbf{X}_{B,j}$ near the tip. These curves can be parametrically represented using quadratic Bézier curves (Fig. 4b) for the subsets preceding and following the tip $\mathbf{X}_{S,j}$, respectively, namely

$$
\begin{aligned}
\overline{\mathbf{X}}^{I}_{j-1}(\xi) &= (1-\xi)^2\mathbf{X}_{S,j-1} + 2(1-\xi)\xi\mathbf{X}^{-}_{S,j} + \xi^2\mathbf{X}_{S,j} \\
\overline{\mathbf{X}}^{I}_{j}(\xi) &= (1-\xi)^2\mathbf{X}_{S,j} + 2(1-\xi)\xi\mathbf{X}^{+}_{S,j} + \xi^2\mathbf{X}_{S,j+1}
\end{aligned}
\tag{18}
$$

Note that the overbar symbol here indicates that the material point belongs to the offset internal boundary $\partial\overline{\Omega}^I$. The two auxiliary vertices $\mathbf{X}^{-}_{S,j}$ and $\mathbf{X}^{+}_{S,j}$ are computed as

$$
\begin{cases}
\mathbf{X}^{-}_{S,j} = \mathbf{X}_{B,j} + \mathbf{s}'_j + \mathbf{s}^{-}_j \\
\mathbf{X}^{+}_{S,j} = \mathbf{X}_{B,j} + \mathbf{s}'_j + \mathbf{s}^{+}_j
\end{cases}
\tag{19}
$$

where

$$
\mathbf{s}'_j = \frac{3s}{2}\frac{(\mathbf{X}_{B,j+1} - \mathbf{X}_{B,j})}{\|\mathbf{X}_{B,j+1} - \mathbf{X}_{B,j}\|}
\tag{20}
$$

and $\mathbf{s}^{-}_j$, $\mathbf{s}^{+}_j$ are calculated by means of Eq. (17), with $s/2$ in place of $\bar{s}$.

The curves start and finish in the main vertices $\mathbf{X}_{S,j-1}$, $\mathbf{X}_{S,j}$, $\mathbf{X}_{S,j+1}$, but do not pass through the auxiliary vertices. Moreover, the two ends of the curves are tangent to the external polygons (fine dashed lines in Fig. 4b), making the opening angle at the tip equal to the angle formed by the vertices $\mathbf{X}^{-}_{S,j}$, $\mathbf{X}_{S,j}$, $\mathbf{X}^{+}_{S,j}$. Thus, the position of the auxiliary vertices can be adjusted in order to generate a desired tip opening angle. The modulus of $\mathbf{s}'_j$, controlling the opening angle at tip, is taken as equal to $3s/2$ to achieve an acute angle.

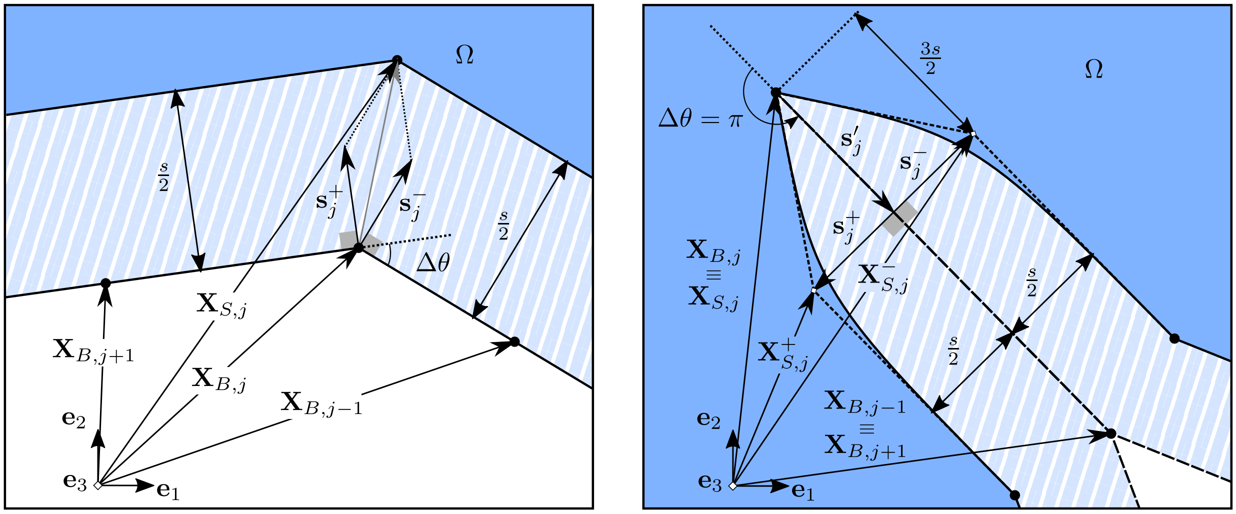

Figure 4. Offset scheme of the internal boundary vertices $\mathbf{X}_{B,j}$. (a) Standard vertex $\mathbf{X}_{B,j}$, (b) vertex $\mathbf{X}_{B,j}$ corresponding to a cut tip.

Among all the possible types of joining dislocations applied to the internal boundary $\partial\Omega^I$, the simplest is the unique "glued" line starting from point A and finishing at point B (see Fig. 3). Accordingly, each pairing $(\partial\overline{\Omega}_i^{I-}, \partial\overline{\Omega}_i^{I+})$, starting from the first element of $\mathcal{V}_S^I$ (point A), is automatically defined by combining the first subset with the last and so forth, with the rule $(\partial\overline{\Omega}_{2N-j+1}^I, \partial\overline{\Omega}_j^I)$, $j = 1, ..., N$. This means that the closure is uniquely defined by point A. In other words, any ordered permutation of the vertices in $\mathcal{V}_S^I$ describes the same inner boundary, but each of them generates a different closure, having different vertices of $\partial\overline{\Omega}^I$ as first element. Thus, since $\mathcal{V}_S^I$ is derived from $\mathcal{V}_B^I$, the latter must be ordered by a proper permutation of vertices, so that the first vertex coincides with the point A of the desired closure.

4.2. Meshing

Element size across the domain is controlled by a function $h(\mathbf{X})$ which provides the average element size for every point $\mathbf{X} \in \Omega$. Geometrical discontinuities represent critical points $\mathbf{X}_P$ that need to be meshed with a suitable refinement. In the algorithm, each vertex of $\partial\overline{\Omega}^I$ contained in the set $\mathcal{V}_S^I$ is treated as a critical point. Accordingly, the global refinement function $h(\mathbf{X})$ is given by $h(\mathbf{X}) = \min_i [h_{P,i}(\mathbf{X})]$, with $h_{P,i}$ being defined as

$$h_{P,i}(\mathbf{X}) = h_{\max} - \frac{h_{\max} - h_{\min}}{\left(\dfrac{\|\mathbf{X} - \mathbf{X}_{P,i}\|^2}{c_k^2} + 1\right)^a} \tag{21}$$

where a is an exponent controlling mesh grading and c_k is a parameter which defines the mesh refinement extension. Note that the function $h_{P,i}(\mathbf{X})$ is such that $h_{P,i}(\mathbf{X}) = h_{\min}$ for $\|\mathbf{X} - \mathbf{X}_{P,i}\| \to 0$, and $h_{P,i}(\mathbf{X}) = h_{\max}$ for $\|\mathbf{X} - \mathbf{X}_{P,i}\| \to \infty$, being $h_{\min}$ and $h_{\max}$ the minimum and the maximum element sizes, respectively.

4.3. Nodal dislocations

The distribution of element nodes along the internal offset boundary $\partial\overline{\Omega}^I$ has to fulfil the refinement function $h(\mathbf{X})$ and the linear mapping function $\Gamma : \partial\overline{\Omega}_i^{I+} \to \partial\overline{\Omega}_i^{I-}$. In order to satisfy both conditions at the same time, nodes are created on the subset requiring the largest number of nodes, and then copied onto the opposite side using the function Γ.

The mean element size along a subset $\partial\overline{\Omega}_i^I$ can be computed using the mean value theorem $h_{m,i} = \int_0^1 h(\overline{\mathbf{X}}_i^I(\xi)) \left\|\partial\overline{\mathbf{X}}_i^I/\partial\xi\right\| \mathrm{d}\xi$. Accordingly, the number of elements along the boundary is given by the ratio between the length of the subset $\partial\overline{\Omega}_i^I$ and the mean element size $h_{m,i}$, namely

$$N_{e,i} = \frac{1}{h_{m,i}} \int_0^1 \left\| \frac{\partial \overline{\mathbf{X}}_i^I}{\partial \xi} \right\| d\xi \ . \tag{22}$$

Nodes are then placed starting from the most critical subset, i.e. that requiring the highest number of elements. The first node, $\mathbf{N}_{i,1} = \overline{\mathbf{X}}_i^I(\xi_1 = 0) \in \partial\overline{\Omega}_i^I$, coincides with the vertex $\mathbf{X}_{S,i}$. From the second node onwards, each node $\mathbf{N}_{i,n}$ is placed along $\partial\overline{\Omega}_i^I$ increasing progressively ξ_n by an arbitrary increment $\Delta\xi$, until the length $\|\mathbf{N}_{i,n} - \mathbf{N}_{i,n-1}\|$ attains the length given by $h(\overline{\mathbf{X}}_i^I(\frac{\xi_n+\xi_{n-1}}{2}))$, so that each element size perfectly matches the dimension defined by the function $h(\mathbf{X})$. After this procedure, the nodes generated are replicated on the pairing subset. So, if nodes have been created first on $\partial\overline{\Omega}_i^{I+}$ their counterparts are replicated on $\partial\overline{\Omega}_i^{I-}$ using $\mathbf{N}_{i,n}^- = \Gamma(\mathbf{N}_{i,n}^+)$. The obtained nodal distribution is now suitable for applying the dislocation constraint, Eq. (14), in a discretised way to each couple of nodes $(\mathbf{N}_{i,n}^-, \mathbf{N}_{i,n}^+)$, $n = 1, 2, ..., N_{e,i}$, for each couple of subsets $(\partial\overline{\Omega}_i^{I-}, \partial\overline{\Omega}_i^{I+})$, $i = 1, ..., N$.

5. Applicative examples

The constitutive model of the hyperelastic wrinkling membrane (Sect. 2.2) has been implemented in the commercial FE code ABAQUS, through a user-defined material subroutine UMAT.

A preliminary verification was performed by comparing the wrinkling model to the standard Ogden model implemented in ABAQUS, under uniaxial tension and uniaxial and equibiaxial compression. As expected, the stress-strain response in uniaxial tension is not influenced by wrinkling (Fig. 5a), while the uniaxial and biaxial compression cases highlight a significant reduction of the compressive stresses due to wrinkling, by one and two orders of magnitude, respectively (Fig. 5b-c).

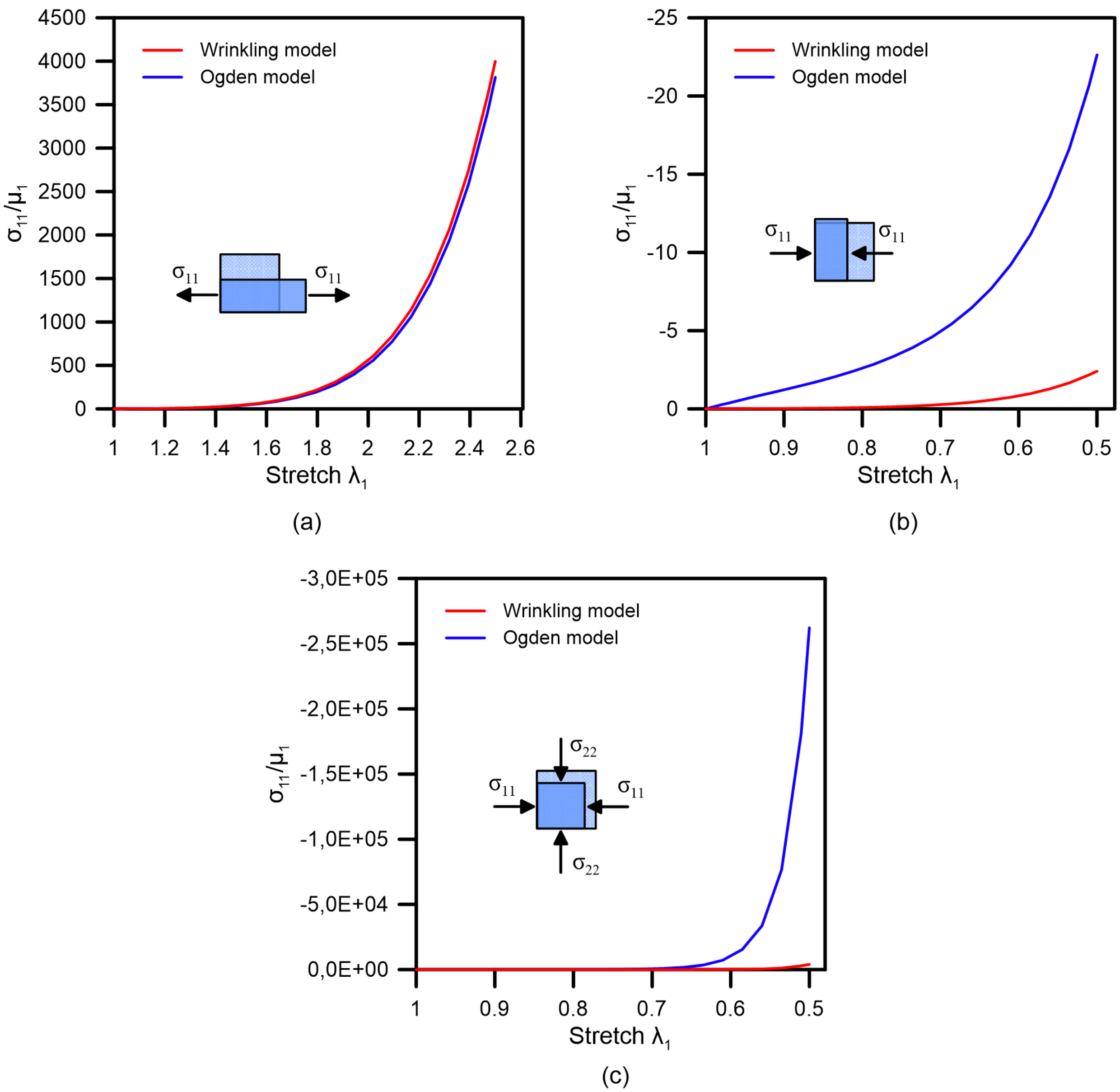

Figure 5. Normalized stress-stretch responses on a single plane stress element analysed with the standard Ogden function Ψ (solid blue line) and that based on the relaxed function Ψ_W, summarized in Tab. 1 (solid red lines). Material parameters: $\mu_1 = 200\,\text{Pa}$, $\alpha_1 = 9$. (a) Uniaxial tension, (b) uniaxial compression, and (c) equibiaxial compression. The slightly stiffer response in (a), as well as the non-zero response under compression in (b) and (c), is due to the introduction of the additional fictitious stiffnessbased on the Ogden function Ψ, with properties $\tilde{\mu} = \mu_1/100$ and $\tilde{\alpha} = \alpha_1$, to prevent ill-conditioning during slackness and wrinkling.

In order to explore the capabilities of the implemented wrinkling model in predicting the non-linear response of hyperelastic membranes, three relevant illustrative examples are presented below. The first one is related to a rectangular polyethylene membrane under bending, which was introduced by Barsotti et al. [49] and later employed by Massabò and Gambarotta [41] to test their wrinkling model. The second example refers to a rectangular silicone membrane containing an elliptical hole under tension, which was tested experimentally by Spagnoli et al. [50]. Finally, in order to verify the capabilities of the proposed algorithm in generating complex internal boundaries, the case of a Z-shaped cut under joining dislocations is presented. This latter case represents an archetypal topology in reconstructive surgery procedures on the human skin, e.g. see Hove et al. [9].

5.1. Rectangular beam under bending

The geometry consists of a rectangular elastomeric beam with span $l =$ 75 mm, height $h = 25$ mm and thickness $t = 1$ mm, laterally constrained along the shorter edge, with imposed displacements $u_2 = -6$ mm applied to the central fifth of the lower edge [49]. The model has been discretised with a uniform mesh of 1700 3-nodes plane stress isoparametric elements (CPS3), with an average size $h_{avg} = 1.5$ mm. The mechanical behaviour of the material was described by Massabò and Gambarotta [41] using an exponential isotropic Fung model. The equivalent Ogden constants, fitted under uniaxial tension, are $\mu_1 = 749.18$ Pa and $\alpha_1 = 17.14$. For the fictitious elasticity tensor $\tilde{\mathbb{C}}^{\boldsymbol{\tau}^\circ}$, $\tilde{\mu} = \mu_1/100$ and $\tilde{\alpha} = \alpha_1$ are used.

Fig. 6 shows the resulting stretch domains, obtained by comparing the wrinkling model with the standard Ogden one. Taut regions, characterised by two positive principal stress components, are highlighted in red, while wrinkled regions, with only one positive principal stress, have been coloured in green. Slack regions where both the principal stresses are negative are blue marked. Note that, using the standard Ogden function, regions are simply identified through the value of the principal stretches, see Tab. 1. The main differences between the two models can be found in the central portion of the membrane. With the standard Ogden model (Fig. 6a), a wide central taut region exists, which is separated from the top slack domain by a small strip of wrinkled membrane. Along the lateral edges, the membrane is taut at top and slack at bottom with a triangular shape. In the case with the wrinkling model (Fig. 6b), the top slack domain extends downward to the taut region, which is here narrower. Furthermore, taut zones near the lateral edges disappear. The domains in Fig. 6b compare qualitatively good with those observed in experiments, see Fig. 6c.

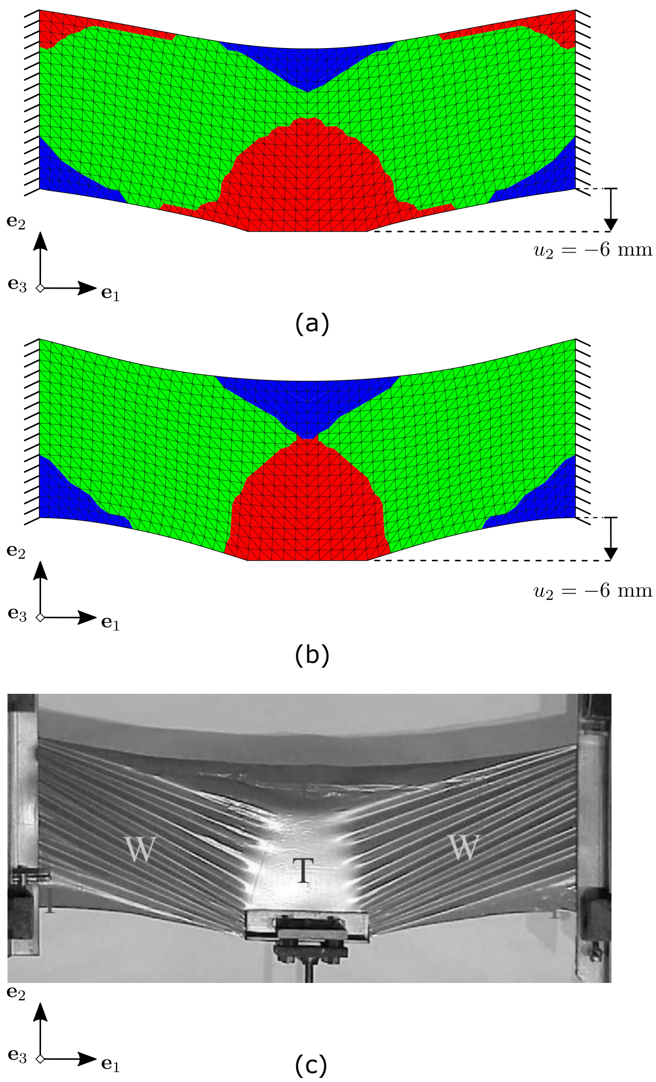

Figure 6. Coloured maps of the taut (red), wrinkled (green) and slack (blue) domains, plotted onto the deformed configuration, in a rectangular membrane analysed with Ogden function (a) and the wrinkling model (b). (c) Experimental test on a clamped rectangular polyethylene membrane conducted by Barsotti et al. [49].

In Fig. 7, the total vertical reaction force along the constrained lower edge is shown against the imposed displacement, showing a relaxation in the situation where the wrinkling model is used.

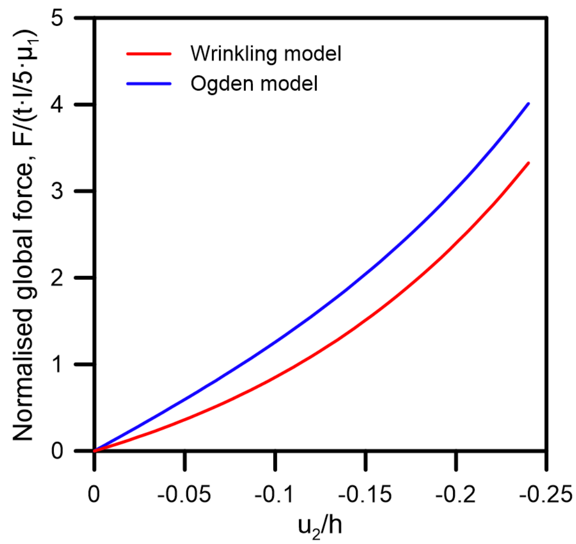

Figure 7. Normalized force-displacement curves of the rectangular beam under bending. The global force F has been divided by the loaded area $l/5 \cdot t$ and normalized with respect to μ_1.

5.2. Notched sheet under tension

The geometry consists of a rectangular silicone polymer sheet with width $l = 117$ mm, height $h = 234$ mm and thickness $t = 2$ mm, containing a centred elliptical notch, with semi-axes $r_1 = 20$ mm and $r_2 = 5$ mm aligned with $\mathbf{e}_1$ and $\mathbf{e}_2$, respectively. The material constants are $\mu_1 = 0.461$ MPa and $\alpha_1 = 2$ [50]. Constants for the fictitious elasticity tensor $\tilde{\mathbb{C}}^{\boldsymbol{\tau}^\circ}$ are taken as in the previous example with $\tilde{\mu} = \mu_1/100$ and $\tilde{\alpha} = \alpha_1$. The membrane is clamped on top and bottom edges and is stretched by applying a vertical displacement $u_2 = 60$ mm, corresponding to a remotely applied stretch of $\lambda_0 \simeq 1.25$. The model has been discretised with 3-nodes plane stress isoparametric elements (CPS3), with a minimum size $h_{min} = 0.6$ mm near the notch, and a maximum size $h_{max} = 5$ mm at the constrained edges.

A comparison of the analyses, conducted using the standard Ogden model and the wrinkling model, is shown in Fig. 8. Both models show a characteristic X-shaped wrinkling region, which seems to extend larger for the membrane analysed with the wrinkling model (Fig. 8b). Slack regions are small and localized near the top and bottom edges of the ellipse. Interestingly, a relevant difference in the shape of the deformed elliptical notch can be appreciated. Initially wider in the horizontal direction, the inner ellipse transforms into a circle upon deformation in the first case (Fig. 8a), and in a vertically extended ellipse in the second (Fig. 8b). This behaviour highlights the effective reduction of the stiffness in compression with the wrinkling model, allowing higher compressive stretches in the transversal direction to develop. From a qualitative point of view, the wrinkling model shows an improved prediction of the actual wrinkling area, which in Fig. 8c is represented by the blue butterfly-like region. In fact, since the vertical E_{22} strain is mostly positive across the domain (Fig. 8d), the sign of the E_{11} component is discriminating in identifying wrinkling areas.

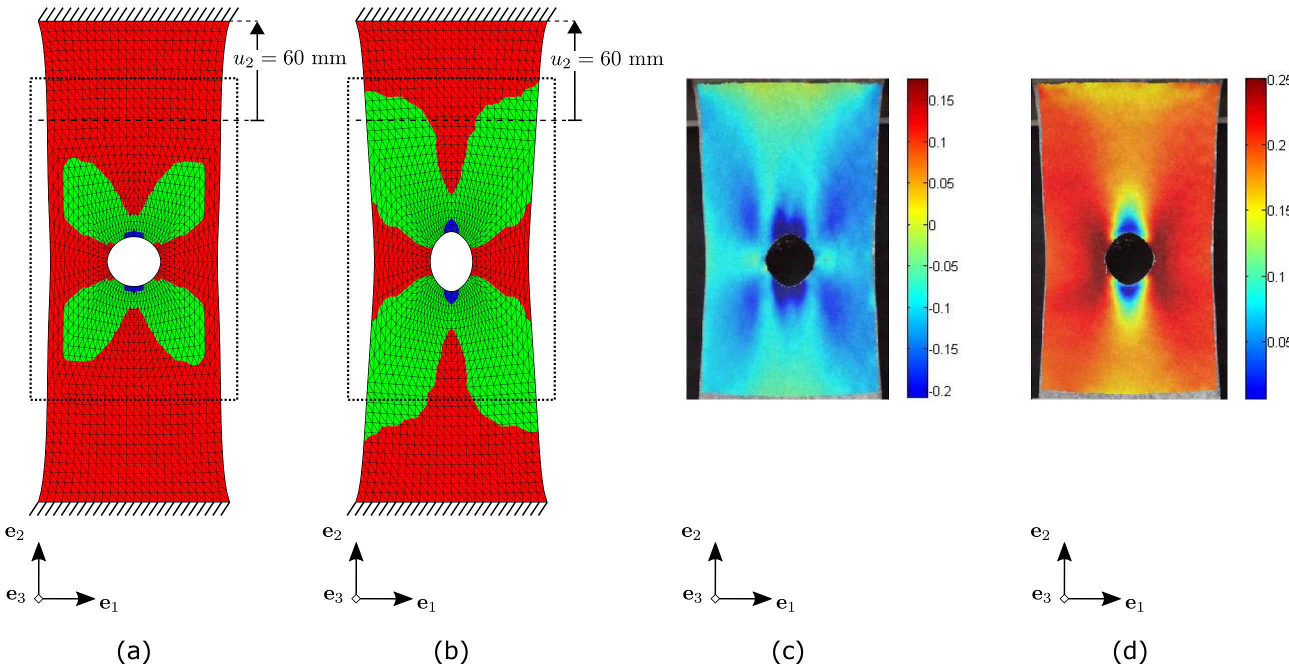

Figure 8. Coloured maps of the taut (red), wrinkled (green) and slack (blue) domains, plotted onto the deformed configuration, in a notched rectangular membrane analysed with Ogden function (a) and the wrinkling model (b). Dotted boxes in (a) and (b) highlight the same area shown in the experimental full-field map of the components E_{11} and E_{22} of the Green-Lagrange strain tensor [50] (c)-(d).

Similarly to the previous example, the total vertical reaction force on the clamped top edge illustrated in Fig. 9 confirms a slight relaxation obtained with the wrinkling model.

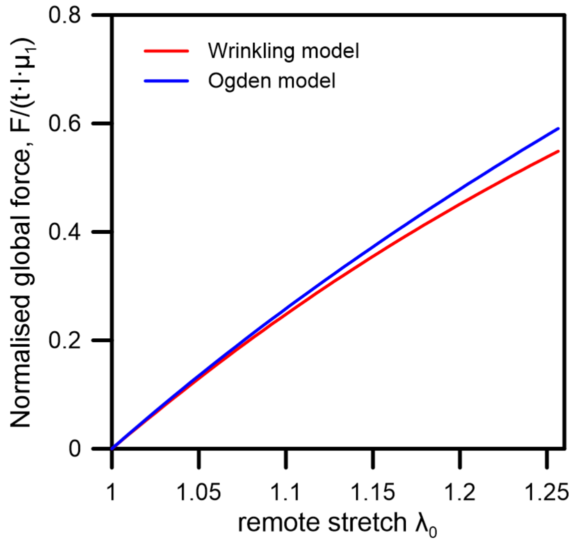

Figure 9. Normalized force-displacement curves of the notched sheet under tension. The global force F has been divided by the section area $l \cdot t$ and normalized with respect to μ_1.

5.3. Z-shaped cut under joining dislocations

A Z-shaped cut under joining dislocations is here analysed. The selected problem is relevant in the field of reconstructive surgery of human skin, where cutting, tissue rearrangement and suturing of skin are performed in order to achieve a desired configuration within the skin membrane. The operation consists in three incisions of equal length, forming a Z-shaped cut, in which the lateral limbs are slanting 60° with respect to the central one [9]. Then, skin is undermined from the subcutaneous tissues and the two resulting triangular flaps are transposed each other and sutured in place. Such a procedure can be simulated by imposing joining dislocation distributions (describing flaps transposition) along an internal boundary (corresponding to the surgical cut). This last example is the benchmark to test the combination of the wrinkling model with the proposed algorithm for describing topologically complex internal boundaries, as presented in Sect. 3.

A circular skin membrane of $R = 100$ mm, containing incisions of $l = 50$ mm, is considered. The domain has been discretised using three-node plane stress isoparametric elements (CPS3), with element size ranging between $h_{\max} = l/5$, $h_{\min} = l/150$ and refinement parameters $a = 8$, $c_k = l$. The cut offset, needed for numerical reasons, is assumed to be equal to $s = h_{max}/20$ (Fig. 10a). The skin parameters are $\mu_1 = 110$ Pa and $\alpha_1 = 26$, taken from the *in-vivo* measurements of Mahmud et al. [51]. The circular external boundary is kept fixed, while the flap transposition is achieved though MPCs prescribed along the two incision sides, according to the dislocation distribution of Eq. (14).

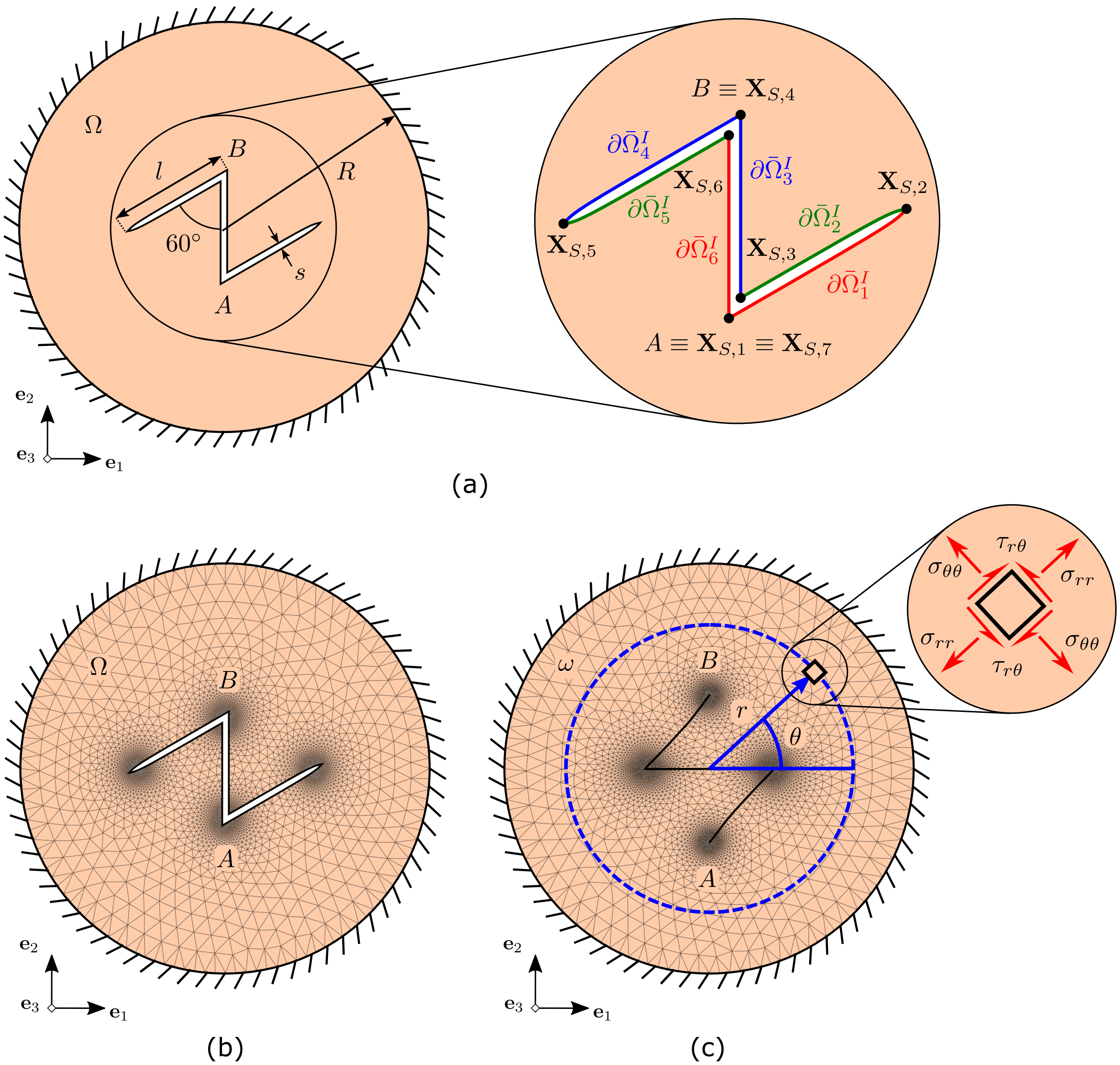

Figure 10. Schematics of the circular membrane with Z-shaped cut before and after the application of joining dislocations. (a) Geometrical description of the problem, with the offset on the cut already applied. Coupled subsets ($\partial\bar{\Omega}_1^{I+} \equiv \partial\bar{\Omega}_1^I$ and $\partial\bar{\Omega}_1^{I-} \equiv \partial\bar{\Omega}_6^I, \partial\bar{\Omega}_2^{I+} \equiv \partial\bar{\Omega}_2^I$ and $\partial\bar{\Omega}_2^{I-} \equiv \partial\bar{\Omega}_5^I, \partial\bar{\Omega}_3^{I+} \equiv \partial\bar{\Omega}_3^I$ and $\partial\bar{\Omega}_3^{I-} \equiv \partial\bar{\Omega}_4^I$) have been highlighted with same colors. (b) Discretised FE model in the reference configuration, and (c) FE model after the analysis with the wrinkling model.

The membrane has been analysed using both the standard Ogden function and the wrinkling model. Contours of the stretch domains, reported in Fig. 11, show a noticeable difference between the two models , being the latter closer to the actual no-compression mechanical behaviour of undermined skin membranes during reconstructive surgery procedures. Slack domains close to the ends of the internal boundaries are much smaller and localised in the case analysed with the wrinkling model. Furthermore, the triangular flaps are predominantly taut, in contrast to the wrinkling predicted by the standard model. However, a narrow region of wrinkles remains throughout the length of the central limb, which extends with two further drop-shaped regions along the same direction.

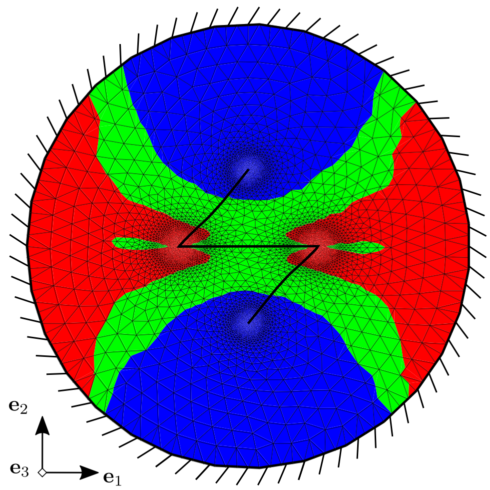

(a)

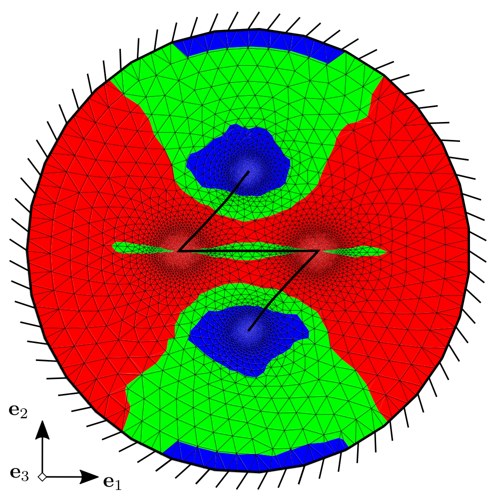

(b)

Figure 11. Coloured maps of the taut (red), wrinkled (green) and slack (blue) domains, plotted onto the deformed configuration, of a Z-shaped cut analysed with Ogden function (a) and the wrinkling model (b).

The distribution of radial stresses along a circular path with $r = 1.5l$ and a radial path for $\theta = 90^\circ$ (refer to Fig. 10c), is reported in Fig. 12 for the two analysed models. The distribution in Fig. 12a is symmetric and highlights an effective reduction of compressive stresses around $\theta = 90°$ and $\theta = 270°$. Indeed, those regions are actually in the slack and wrinkled domain, and the red curve remains at a constant stress value of $\sigma_{rr} \simeq 0$. Looking at the radial distribution at $\theta = 90°$ (Fig. 12b), the membrane analysed with the standard Ogden function shows negative stresses along the whole path, displaying a peak at $r = 35$ mm representing the point B. The wrinkling model, instead, presents an almost constant distribution around $\sigma_{rr} = 0$, with just a small zone, near $r = 10$ mm, having positive stresses.

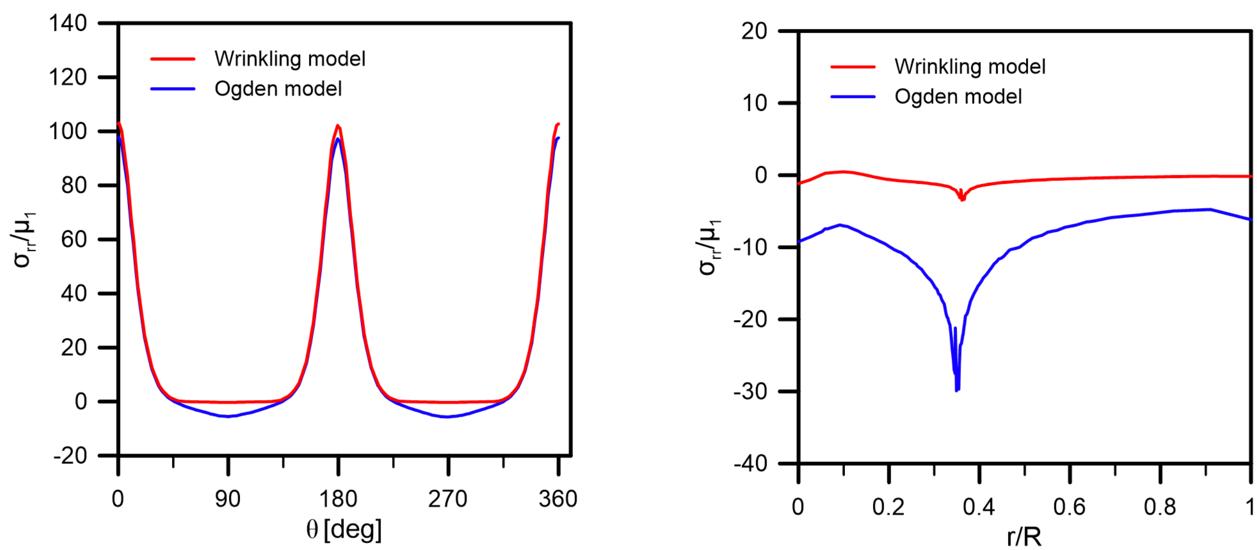

(a) (b)

Figure 12. Normalized radial stress σ_{rr} distribution along (a) a circular path with radius $R = 1.5l$, and (b) a radial path with angle $\theta = 90°$ of the Z-shaped cut with the standard Ogden function and the wrinkling model.

6. Discussion and conclusions

The analysis of soft tissue membranes using numerical methods is a fundamental step in order to understand the mechanical behaviour of these thin structures under particular loading conditions, such as closure of holes and cuts. This is achieved by applying joining dislocations on the inner boundaries, that is, enforcing two distinct edges to move towards each other, with reciprocal forces, until the overlap is reached, while maintaining a self-balanced stress field during the whole process. In this work, a FE framework is adopted, in which the closure is simulated with Multi-Point Constraints (MPCs) applied to the nodes of the inner boundaries. To meet the requirements of a refined discretisation near geometrical discontinuities, and the necessities of MPCs to have evenly discretised coupling edges, a pre-processing algorithm for automatic FE models generation has been formulated and implemented in Matlab® environment. The code developed offers five main advantages with respect to existing solutions: (i) the automatic mesh generating code offers wide control on discretisation management; (ii) the geometries are discretised with a high-quality mesh; (iii) the domain geometry can be generated parametrically, minimising user-requiring inputs; (iv) nodes on the holes and cuts boundary are consistently distributed for MPCs; finally, (v) the time required to generate models is greatly reduced.

With respect to the mechanical behaviour of the soft tissues, this has been considered using the well-known isotropic Ogden's strain-energy function. In order to consider the instability of membranes subjected to compressive forces, also known as wrinkling, the function has been modified, treating the out-of-plane displacements of the actual wrinkles as material non-linearities.

Although this approach cannot provide a detailed description of the actual waves and wrinkles, it represents a highly efficient way to obtain a good approximation of the overall tension field within the membrane, avoiding the problems of stability and convergence of buckling and post-buckling analyses.

The examples presented have been carefully selected in order to illustrate the potential of the proposed algorithm, both in accurately simulating membranes undergoing wrinkling and in precisely describing the application of general dislocation distributions along topologically complex internal boundaries. All the examples showed a redistribution of the stress and strain fields when analysed with the wrinkling function, observing a relevant improvement in the qualitative prediction of the taut-wrinkling-slack regions in the example of the membrane tested by Barsotti et al. [49]. In the case of a Z-shaped cut, the slack region is significantly reduced, highlighting the capability of the wrinkling model to redistribute compression stresses into tensions in other membrane regions to achieve equilibrium. The closure of the cut, which induced the transposition of the triangular flaps, has been achieved automatically during the FE computation, without convergence problems.

The proposed code is robust, and can generate cuts and holes of whichever shape with high efficiency. However, further improvements are planned in order to include the analysis of multiple holes, as well as layered and curved membranes. This can be done without changing the basic theory of closing holes herein presented, as it has been formulated for membranes placed in $\mathbb{R}^3$ presenting n holes. As a result, the range of possible applications will be further expanded, for instance to simulate kirigami tessellations [12], dorsal closure of drosophila embryos [52], or the V-Y advancement flap in facial reconstructive surgery [53], to mention only a few relevant examples.

7. Declaration of Competing Interest

The authors declare no potential conflicts of interest with respect to the research, authorship, and/or publication of this article.

Appendix A. Structure of the algorithm

As described in Sect. 4, the proposed algorithm combines auto-meshing and generation of complex dislocation distributions in Matlab® environment, employing the open source auto-meshing tool DistMesh. The general structure of the code, composed of seven main functions, is shown in Tab. 1. The main functions are described in detail below.

Table 1: Structure of the code

geometry shapes : E_{shape}, I_{shape}

geometry parameters: $\{E_{p1}, E_{p2}, ...\}$, $\{I_{p1}, I_{p2}, ...\}$, t, s

mesh parameters : h_{min}, h_{max} ,a ,c_k

material properties : μ_i, α_i

pre-stress tensor : $\boldsymbol{\sigma}_0$

1: $\mathcal{V}_B^E$, $\mathcal{V}_B^I \leftarrow$ **call** GeomBoundaries(E_{shape},I_{shape},$\{E_{p1}, E_{p2}, ...\}$,$\{I_{p1}, I_{p2}, ...\}$);

2: $\mathcal{V}_S^I \leftarrow$ **call** InternalOffset($\mathcal{V}_B^I$,s);

3: $d(\mathbf{X})$ = SignedDistance($\mathbf{X}$,$\mathcal{V}_B^E$,$\mathcal{V}_S^I$);

4: $h(\mathbf{X})$ = ElementSize($\mathbf{X}$,$\mathcal{V}_S^I$,h_{min}, h_{max} ,a ,c_k);

5: $\mathcal{V}_N^{I-}$, $\mathcal{V}_N^{I+} \leftarrow$ **call** InternalBoundaryNodes($h(\mathbf{X})$,$\mathcal{V}_S^I$,$\mathcal{V}_B^I$);

6: $\mathcal{V}_N$, $\mathcal{C} \leftarrow$ **call** DistMesh($d(\mathbf{X})$,$h(\mathbf{X})$,$\{\mathcal{V}_N^{I-}, \mathcal{V}_N^{I+}, \mathcal{V}_B^E\}$);

7: **call** PrintInputABQ($\mathcal{V}_N$,$\mathcal{C}$,t,μ_i, α_i,$\mathcal{V}_N^{I-}$,$\mathcal{V}_N^{I+}$,$\boldsymbol{\sigma}_0$);

Initially, all the information about geometry, element size, material properties and pre-stress field, is read. Note that this is the only code section requiring user input. Depending on the shape chosen for the outer boundary through the text variable E_{shape} (or I_{shape} for the inner boundary), the first main function GeomBoundaries (Tab. 2) computes the set of external boundary vertices $\mathcal{V}_B^E$ (internal boundary vertices $\mathcal{V}_B^I$), addressing the task to the proper function ExtShape-n (IntShape-n) and taking the set of geometrical parameters $\{E_{p1}, E_{p2}, ...\}$ ($\{I_{p1}, I_{p2}, ...\}$) as input.

Table 2: Definition of external and internal boundaries

Function GEOMBOUNDARIES(E_{shape},I_{shape},$\{E_{p1}, E_{p2}, ...\}$,$\{I_{p1}, I_{p2}, ...\}$)

  switch E_{shape} **do** compute the set $\mathcal{V}_B^E$

    case ($external\ shape$ 1) **do**

      $\mathcal{V}_B^E \leftarrow$ **call** EXTSHAPE-1($\{E_{p1}, E_{p2}, ...\}$)

    case ($external\ shape$ 2) **do**

      $\mathcal{V}_B^E \leftarrow$ **call** EXTSHAPE-2($\{E_{p1}, E_{p2}, ...\}$)

    ...

  switch I_{shape} **do** compute the set $\mathcal{V}_B^I$

    case ($internal\ shape$ 1) **do**

      $\mathcal{V}_B^I \leftarrow$ **call** INTSHAPE-1($\{I_{p1}, I_{p2}, ...\}$)

    case ($internal\ shape$ 2) **do**

      $\mathcal{V}_B^I \leftarrow$ **call** INTSHAPE-2($\{I_{p1}, I_{p2}, ...\}$)

    ...

  return $\mathcal{V}_B^E$,$\mathcal{V}_B^I$

The second main function, INTERNALOFFSET (Tab. 3), performs the offset of the internal boundaries as described in Sect. 4.1, generating the set $\mathcal{V}_S^I$ from $\mathcal{V}_B^I$.

Table 3: Offset of internal boundary vertices

Function INTERNALOFFSET($\mathcal{V}_B^I$,s)
  foreach $\left(\mathbf{X}_{B,j} \in \mathcal{V}_B^I\right)$ **do**
    Compute the angle $\Delta\theta$ at the vertex $\mathbf{X}_{B,j}$ between the segments $\mathbf{X}_{B,j} - \mathbf{X}_{B,j-1}$ and $\mathbf{X}_{B,j+1} - \mathbf{X}_{B,j}$;
    if $(\Delta\theta = \pi)$ **then**
      Compute $\mathbf{s}_j^-$, $\mathbf{s}_j^+$, $\mathbf{s}_j^{'}$ using Eqs. (17) and (20) with $\bar{s} = s/2$;
      Set $\mathbf{X}_{S,j} \equiv \mathbf{X}_{B,j}$;
      Compute $\mathbf{X}_{S,j}^-$, $\mathbf{X}_{S,j}^+$ using Eqs. (19);
      Enqueue the set $\left\{\mathbf{X}_{S,j}^-, \mathbf{X}_{S,j}, \mathbf{X}_{S,j}^+\right\}$ into $\mathcal{V}_S^I$;
    else
      Compute $\mathbf{s}_j^-$, $\mathbf{s}_j^+$ using Eq. (17) with $\bar{s} = s/(2(1 + \cos\Delta\theta))$;
      Compute $\mathbf{X}_{S,j}$ using Eq. (16);
      Enqueue $\mathbf{X}_{S,j}$ into $\mathcal{V}_S^I$;
  return $\mathcal{V}_S^I$

The third main function, SIGNEDDISTANCE, computes the signed distance function $d(\mathbf{X})$, giving as output negative numbers for points $\mathbf{X}$ inside the domain, and positive elsewhere. It is a fundamental argument for the DistMesh auto-meshing tool as it identifies the region to mesh, and it is defined by subtraction of the two surfaces enclosed within the external and internal boundaries. More details about this function can be found in [34]. The fourth main function, ELEMENTSIZE (Tab. 4), provides $h(\mathbf{X})$, the element size parameter required in order to refine the mesh around geometrical discontinuities. According to Sect. 4.2, the function refines the mesh around each vertex $\mathbf{X}_{S,j} \in \mathcal{V}_S^I$.

Table 4: Mesh refinement

Function ElementSize($\mathbf{X}$,$\mathcal{V}_S^I$,h_{min}, h_{max} ,a ,c_k)
- **foreach** $\left(\mathbf{X}_{S,j} \in \mathcal{V}_S^I\right)$ **do**
  - Compute element dimension $h_{S,j}$ in $\mathbf{X}$ according to the refinement function for the vertex $\mathbf{X}_{S,j}$ using Eq. (21);
- Compute element dimension in $\mathbf{X}$ as the minimum $h_{S,j}$ value: $h = \min_j [h_{S,j}]$;
- **return** h

Internal boundary nodes are generated following the procedure described in Sect. 4.3 through the main function InternalBoundaryNodes, and stored into the sets $\mathcal{V}_N^{I-}$, $\mathcal{V}_N^{I+}$, pertaining to the left and right boundary sides, respectively.

Table 5: Generation of internal boundary nodes

1: **Function** InternalBoundaryNodes$(h(\mathbf{X}), \mathcal{V}_S^I, \mathcal{V}_B^I)$
2: $\quad N \leftarrow (\text{size}(\mathcal{V}_B^I) - 1)/2$ number of coupled internal boundary subsets $(\partial\overline{\Omega}_i^{I-}, \partial\overline{\Omega}_i^{I+})$;
3: $\quad$ Set as first elements of $\mathcal{V}_N^{I-}$ and $\mathcal{V}_N^{I+}$ the first vertex of $\mathcal{V}_S^I$, i.e. A;
4: $\quad \mathbf{N}_{k^-,n-1}, \mathbf{N}_{k^+,n-1} \leftarrow A$;
5: $\quad$ **for** $j \leftarrow 1$ **to** N **do**
6: $\quad\quad$ Use the subset matching rule $(\partial\overline{\Omega}_{k^-}^I, \partial\overline{\Omega}_{k^+}^I)$, where $k^+ = j$ and $k^- = 2N - j + 1$;
7: $\quad\quad \overline{\mathbf{X}}_{k^-}^I(\xi) =$ BézierCurve$(\xi, k^-, \mathcal{V}_S^I)$;
8: $\quad\quad \overline{\mathbf{X}}_{k^+}^I(\xi) =$ BézierCurve$(\xi, k^+, \mathcal{V}_S^I)$;
9: $\quad\quad$ Compute the numbers of elements N_{e,k^-}, N_{e,k^+} required to discretize $\partial\overline{\Omega}_{k^-}^I$ and $\partial\overline{\Omega}_{k^+}^I$, respectively, using Eq. (22);
10: $\quad\quad \xi_{n-1}, \xi_n \leftarrow 0$;
11: $\quad\quad$ **if** $(N_{e,k^+} \geq N_{e,k^-})$ **then** generate nodes on $\partial\overline{\Omega}_{k^+}^I$ and replicate them on $\partial\overline{\Omega}_{k^-}^I$:
12: $\quad\quad\quad$ **while** $(\xi_n \leq 1)$ **do**
13: $\quad\quad\quad\quad$ **while** $(\xi_n \leq 1)$ **do**
14: $\quad\quad\quad\quad\quad \xi_n \leftarrow \xi_n + \Delta\xi$;
15: $\quad\quad\quad\quad\quad \mathbf{N}_{k^+,n} \leftarrow \overline{\mathbf{X}}_{k^+}^I(\xi_n)$;
16: $\quad\quad\quad\quad\quad$ **if** $\left(\|\mathbf{N}_{k^+,n} - \mathbf{N}_{k^+,n-1}\| \geq h(\mathbf{X}_{k^+}^I(\frac{\xi_n + \xi_{n-1}}{2}))\right)$ **then** Exit loop;
17: $\quad\quad\quad\quad \mathbf{N}_{k^-,n} = \Gamma(\mathbf{N}_{k^+,n})$;
18: $\quad\quad\quad\quad$ Enqueue $\mathbf{N}_{k^+,n}$ and $\mathbf{N}_{k^-,n}$ into $\mathcal{V}_N^{I+}$ and $\mathcal{V}_N^{I-}$, respectively;
19: $\quad\quad\quad\quad \xi_{n-1} \leftarrow \xi_n$;
20: $\quad\quad\quad\quad \mathbf{N}_{k^+,n-1} \leftarrow \mathbf{N}_{k^+,n}$ and $\mathbf{N}_{k^-,n-1} \leftarrow \mathbf{N}_{k^-,n}$;
21: $\quad\quad$ **else if** $(N_{e,k^+} < N_{e,k^-})$ **then** generate nodes on $\partial\overline{\Omega}_{k^-}^I$ and replicate them on $\partial\overline{\Omega}_{k^+}^I$:
22: $\quad\quad\quad$ Do the same operations from line 12 to 20, but on the k^--th subset;
23: $\quad$ **return** $\mathcal{V}_N^{I+}, \mathcal{V}_N^{I-}$

Parametric functions $\overline{\mathbf{X}}_{k^-}^I(\xi)$, $\overline{\mathbf{X}}_{k^+}^I(\xi)$, in lines 8 and 7 of Tab. 5, are defined by BézierCurve, shown in Tab. 6.

Table 6: Bézier curve definition

Function BézierCurve(ξ,k,$\mathcal{V}_S^I$)
  if $\left(\mathbf{X}_{S,k+1}^{-}\right.$ is between $\mathbf{X}_{S,k}$ and $\left.\mathbf{X}_{S,k+1}\right)$ **then**
    use quadratic Bézier curve from Eq. (18)a:
      $\mathbf{X} = \overline{\mathbf{X}}_k^I(\xi) = (1-\xi)^2\mathbf{X}_{S,k} + 2(1-\xi)\xi\mathbf{X}_{S,k+1}^{-} + \xi^2\mathbf{X}_{S,k+1}$;
  else if $\left(\mathbf{X}_{S,k}^{+}\right.$ is between $\mathbf{X}_{S,k}$ and $\left.\mathbf{X}_{S,k+1}\right)$ **then**
    use quadratic Bézier curve from Eq. (18)b:
      $\mathbf{X} = \overline{\mathbf{X}}_k^I(\xi) = (1-\xi)^2\mathbf{X}_{S,k} + 2(1-\xi)\xi\mathbf{X}_{S,k}^{+} + \xi^2\mathbf{X}_{S,k+1}$;
  else use linear Bézier curve from Eq. (15):
      $\mathbf{X} = \overline{\mathbf{X}}_k^I(\xi) = (1-\xi)\mathbf{X}_{S,k} + \xi\mathbf{X}_{S,k+1}$;
  return X

After computing the required variables, automeshing begins. Nodes in $\mathcal{V}_N^{I-}$, $\mathcal{V}_N^{I+}$, $\mathcal{V}_B^E$ are fixed, i.e. they do not change their position over DistMesh iterations to find the optimal discretization. Once convergence is reached, the set $\mathcal{V}_N$ containing all nodes, and the connectivity matrix $\mathcal{C}$, are given as output. Then, all the information can be printed in an input file for any FE solver. In this work, the input file is written for ABAQUS commercial software using the PrintInputABQ function.

References

[1] H. Watson, Biological membranes, Essays in Biochemistry 59 (2015) 43–69. doi:10.1042/bse0590043.

[2] F. Martini, J. L. Nath, Anatomy & Physiology, Benjamin Cummings, 2010.

[3] A. Chanda, V. Unnikrishnan, Z. Flynn, K. Lackey, Experimental study on tissue phantoms to understand the effect of injury and suturing on human skin mechanical properties, Proceedings of the Institution of Mechanical Engineers, Part H: Journal of Engineering in Medicine 231 (2017) 80–91. doi:10.1177/0954411916679438.

[4] G. Lorenz, A. Kandelbauer, Silicones, in: Handbook of Thermoset Plastics, Elsevier, 2014, pp. 555–575. doi:10.1016/B978-1-4557-3107-7.00014-2.

[5] Y. Zhang, Y. Huang, J. A. Rogers, Mechanics of stretchable batteries and supercapacitors, Current Opinion in Solid State and Materials Science 19 (2015) 190–199. doi:10.1016/j.cossms.2015.01.002.

[6] Z. Yi, L. G. Bettini, G. Tomasello, P. Kumar, P. Piseri, I. Valitova, P. Milani, F. Soavi, F. Cicoira, Flexible conducting polymer transistors with supercapacitor function, Journal of Polymer Science Part B: Polymer Physics 55 (2017) 96–103. doi:10.1002/polb.24244.

[7] A. B. Tepole, H. Kabaria, K.-U. Bletzinger, E. Kuhl, Isogeometric Kirchhoff–Love shell formulations for biological membranes, Computer Methods in Applied Mechanics and Engineering 293 (2015) 328–347. doi:10.1016/j.cma.2015.05.006.

[8] T. Lee, A. K. Gosain, I. Bilionis, A. B. Tepole, Predicting the effect of aging and defect size on the stress profiles of skin from advancement,

rotation and transposition flap surgeries, Journal of the Mechanics and Physics of Solids 125 (2019) 572–590. doi:10.1016/j.jmps.2019.01.012.

[9] C. R. Hove, E. F. Williams, III, B. J. Rodgers, Z-Plasty: A Concise Review, Facial Plastic Surgery 17 (2001) 289–294. doi:10.1055/s-2001-18828.

[10] D. Yan, K. Zhang, F. Peng, G. Hu, Tailoring the wrinkle pattern of a microstructured membrane, Applied Physics Letters 105 (2014) 071905. doi:10.1063/1.4893596.

[11] Z. Yan, F. Zhang, J. Wang, F. Liu, X. Guo, K. Nan, Q. Lin, M. Gao, D. Xiao, Y. Shi, Y. Qiu, H. Luan, J. H. Kim, Y. Wang, H. Luo, M. Han, Y. Huang, Y. Zhang, J. A. Rogers, Controlled Mechanical Buckling for Origami-Inspired Construction of 3D Microstructures in Advanced Materials, Advanced Functional Materials 26 (2016) 2629–2639. doi:10.1002/adfm.201504901.

[12] G. P. T. Choi, L. H. Dudte, L. Mahadevan, Programming shape using kirigami tessellations, Nature Materials 18 (2019) 999–1004. doi:10.1038/s41563-019-0452-y.

[13] W. F. Larrabee, J. A. Galt, A finite element model of skin deformation. III. The finite element model, The Laryngoscope 96 (1986) 413–419. doi:10.1288/00005537-198604000-00014.

[14] D. Lott-Crumpler, H. Chaudhry, Optimal patterns for suturing wounds

of complex shapes to foster healing, Journal of Biomechanics 34 (2001) 51–58. doi:10.1016/S0021-9290(00)00160-3.

[15] C. Flynn, Finite element models of wound closure, Journal of Tissue Viability 19 (2010) 137–149. doi:10.1016/j.jtv.2009.10.001.

[16] A. Rajabi, A. T. Dolovich, J. Johnston, From the rhombic transposition flap toward Z-plasty: An optimized design using the finite element method, Journal of Biomechanics 48 (2015) 3672–3678. doi:10.1016/j.jbiomech.2015.08.021.

[17] O. C. Zienkiewicz, R. L. Taylor, D. Fox, The Finite Element Method for Solid and Structural Mechanics, Elsevier Science, Amsterdam, 2014.

[18] X. F. Wang, Q. S. Yang, S.-s. Law, Wrinkled membrane element based on the wrinkling potential, International Journal of Solids and Structures 51 (2014) 3532–3548. doi:10.1016/j.ijsolstr.2014.06.004.

[19] M. Trejo, C. Douarche, V. Bailleux, C. Poulard, S. Mariot, C. Regeard, E. Raspaud, Elasticity and wrinkled morphology of Bacillus subtilis pellicles, Proceedings of the National Academy of Sciences 110 (2013) 2011–2016. doi:10.1073/pnas.1217178110.

[20] G. Limbert, E. Kuhl, On skin microrelief and the emergence of expression micro-wrinkles, Soft Matter 14 (2018) 1292–1300. doi:10.1039/C7SM01969F.

[21] F. D. Fischer, F. G. Rammerstorfer, N. Friedl, W. Wieser, Buckling phenomena related to rolling and levelling of sheet metal, Inter-

national Journal of Mechanical Sciences 42 (2000) 1887–1910. doi:10.1016/S0020-7403(99)00079-X.

[22] G. Bolzon, M. Shahmardani, R. Liu, E. Zappa, Failure analysis of thin metal foils, Frattura ed Integrità Strutturale 11 (2017) 328–336. doi:10.3221/IGF-ESIS.42.34.

[23] P. Plucinsky, K. Bhattacharya, Microstructure-enabled control of wrinkling in nematic elastomer sheets, Journal of the Mechanics and Physics of Solids 102 (2017) 125–150. doi:10.1016/j.jmps.2017.02.009. arXiv:1611.08621.

[24] P. Harrison, L. F. Gonzalez Camacho, Deep draw induced wrinkling of engineering fabrics, International Journal of Solids and Structures 212 (2021) 220–236. doi:10.1016/j.ijsolstr.2020.12.003.

[25] T. Iwasa, M. C. Natori, K. Higuchi, Evaluation of Tension Field Theory for Wrinkling Analysis With Respect to the Post-Buckling Study, Journal of Applied Mechanics 71 (2004) 532–540. doi:10.1115/1.1767171.

[26] V. Nayyar, K. Ravi-Chandar, R. Huang, Stretch-induced stress patterns and wrinkles in hyperelastic thin sheets, International Journal of Solids and Structures 48 (2011) 3471–3483. doi:10.1016/j.ijsolstr.2011.09.004.

[27] S. Abdelkhalek, H. Zahrouni, N. Legrand, M. Potier-Ferry, Post-buckling modeling for strips under tension and residual stresses using asymptotic numerical method, International Journal of Mechanical Sciences 104 (2015) 126–137. doi:10.1016/j.ijmecsci.2015.10.011.

[28] C. Fu, T. Wang, F. Xu, Y. Huo, M. Potier-Ferry, A modeling and resolution framework for wrinkling in hyperelastic sheets at finite membrane strain, Journal of the Mechanics and Physics of Solids 124 (2019) 446–470. doi:10.1016/j.jmps.2018.11.005.

[29] D. G. Roddeman, J. Drukker, C. W. J. Oomens, J. D. Janssen, The Wrinkling of Thin Membranes: Part I—Theory, Journal of Applied Mechanics 54 (1987) 884–887. doi:10.1115/1.3173133.

[30] L. Gambarotta, R. Massabò, R. Morbiducci, E. Raposio, P. Santi, In vivo experimental testing and model identification of human scalp skin, Journal of Biomechanics 38 (2005) 2237–2247. doi:10.1016/j.jbiomech.2004.09.034.

[31] A. Jarasjarungkiat, R. Wüchner, K.-U. Bletzinger, A wrinkling model based on material modification for isotropic and orthotropic membranes, Computer Methods in Applied Mechanics and Engineering 197 (2008) 773–788. doi:10.1016/j.cma.2007.09.005.

[32] S. L. Evans, On the implementation of a wrinkling, hyperelastic membrane model for skin and other materials, Computer Methods in Biomechanics and Biomedical Engineering 12 (2009) 319–332. doi:10.1080/10255840802546762.

[33] A. Patil, A. Nordmark, A. Eriksson, Instabilities of wrinkled membranes with pressure loadings, Journal of the Mechanics and Physics of Solids 94 (2016) 298–315. doi:10.1016/J.JMPS.2016.05.014.

[34] P. Persson, G. Strang, A Simple Mesh Generator in MATLAB, Society for Industrial and Applied Mathematics 46 (2004) 329–345.

[35] G. A. Holzapfel, R. Eberlein, P. Wriggers, H. W. Weizsäcker, Large strain analysis of soft biological membranes: Formulation and finite element analysis, Computer Methods in Applied Mechanics and Engineering 132 (1996) 45–61. doi:10.1016/0045-7825(96)00999-1.

[36] V. Prot, B. Skallerud, G. A. Holzapfel, Transversely isotropic membrane shells with application to mitral valve mechanics. Constitutive modelling and finite element implementation, International Journal for Numerical Methods in Engineering 71 (2007) 987–1008. doi:10.1002/nme.1983.

[37] G. A. Holzapfel, Nonlinear Solid Mechanics: A Continuum Approach for Engineering Science, Wiley, Chichester, 2000.

[38] R. W. Ogden, Large Deformation Isotropic Elasticity - On the Correlation of Theory and Experiment for Incompressible Rubberlike Solids, Proceedings of the Royal Society A: Mathematical, Physical and Engineering Sciences 326 (1972) 565–584. doi:10.1098/rspa.1972.0026.

[39] O. A. Shergold, N. A. Fleck, Mechanisms of deep penetration of soft solids, with application to the injection and wounding of skin, Proceedings of the Royal Society A: Mathematical, Physical and Engineering Sciences 460 (2004) 3037–3058. doi:10.1098/rspa.2004.1315.

[40] A. C. Pipkin, Relaxed energy densities for large deformations of membranes, IMA Journal of Applied Mathematics 52 (1994) 297–308. doi:10.1093/imamat/52.3.297.

[41] R. Massabò, L. Gambarotta, Wrinkling of Plane Isotropic Biological Membranes, Journal of Applied Mechanics 74 (2007) 550. doi:10.1115/1.2424240.

[42] J. E. Marsden, T. J. R. Hughes, Mathematical Foundations of Elasticity, Dover Civil and Mechanical Engineering Series, Dover, 1994.

[43] S. J. Connolly, D. Mackenzie, Y. Gorash, Isotropic hyperelasticity in principal stretches: explicit elasticity tensors and numerical implementation, Computational Mechanics 64 (2019) 1273–1288. doi:10.1007/s00466-019-01707-1.

[44] T. J. R. Hughes, J. Winget, Finite rotation effects in numerical integration of rate constitutive equations arising in large-deformation analysis, International Journal for Numerical Methods in Engineering 15 (1980) 1862–1867. doi:10.1002/nme.1620151210.

[45] M. Palizi, S. Federico, S. Adeeb, Consistent numerical implementation of hypoelastic constitutive models, Zeitschrift für angewandte Mathematik und Physik 71 (2020) 156. doi:10.1007/s00033-020-01335-3.

[46] V. Volterra, Sur l'équilibre des corps élastiques multiplement connexes 24 (1907) 401–517.

[47] C. Somigliana, Sulla teoria delle distorsioni elastiche, Il Nuovo Cimento (1911-1923) 11 (1916) 177–192.

[48] B. A. Bilby, John Douglas Eshelby. 21 december 1916-10 december 1981, Biographical Memoirs of Fellows of the Royal Society 36 (1990) 127–150.

[49] R. Barsotti, S. S. Ligarò, G. F. Royer-Carfagni, The web bridge, International Journal of Solids and Structures 38 (2001) 8831–8850. doi:10.1016/S0020-7683(01)00115-9.

[50] A. Spagnoli, M. Terzano, R. Brighenti, F. Artoni, A. Carpinteri, How Soft Polymers Cope with Cracks and Notches, Applied Sciences 9 (2019) 1086. doi:10.3390/app9061086.

[51] L. Mahmud, N. F. Adull Manan, M. H. Ismail, J. Mahmud, Characterisation of soft tissues biomechanical properties using 3D Numerical Approach, in: 2013 IEEE Business Engineering and Industrial Applications Colloquium (BEIAC), volume 3, IEEE, 2013, pp. 801–806. doi:10.1109/BEIAC.2013.6560246.

[52] L. Almeida, P. Bagnerini, A. Habbal, S. Noselli, F. Serman, A mathematical model for dorsal closure, Journal of Theoretical Biology 268 (2011) 105–119. doi:10.1016/j.jtbi.2010.09.029.

[53] E. G. Zook, A. L. Van Beek, R. C. Russell, J. B. Moore, V-Y Advancement Flap for Facial Defects, Plastic and Reconstructive Surgery 65 (1980) 786–797. doi:10.1097/00006534-198006000-00011.